THESIS FOR THE DEGREE OF DOCTOR OF PHILOSOPHY

Experimental Development of Distributed Optical Fibre Monitoring Methods for Underground Infrastructure

August Jansson

Department of Architecture and civil engineering
Chalmers University of Technology
Gothenburg, Sweden, 2026

Experimental Development of Distributed Optical Fibre Monitoring Methods for Underground Infrastructure

August Jansson
ISBN 978-91-8103-482-0
DOI https://doi.org/10.63959/chalmers.dt/5939

Acknowledgements, dedications, and similar personal statements in this thesis, reflect the author's own views.

© August Jansson 2026 except where otherwise stated.

Doktorsavhandlingar vid Chalmers tekniska högskola
Ny serie nr 5939
ISSN 0346-718X

Department of Architecture and civil engineering
Chalmers University of Technology
SE-412 96 Gothenburg, Sweden
Phone: +46 (0)31 772 1000

Cover:
A section of a tunnel instrumented with both monitoring applications developed in this thesis.

Printed by Chalmers Digital Printing
Gothenburg, Sweden, September 2026

Experimental Development of Distributed Optical Fibre Monitoring Methods for Underground Infrastructure

August Jansson
Department of Architecture and civil engineering
Chalmers University of Technology

Abstract

Monitoring during underground construction is essential for verifying design assumptions, assessing structural behaviour, and supporting safe and efficient excavation. However, conventional monitoring methods are often limited to discrete measurement points, which may be insufficient for identifying localised deformation and load-transfer mechanisms in jointed rock masses and tunnel support systems. This thesis investigates the use of distributed optical fibre sensors (DOFS) for high-resolution strain-based monitoring in hard rock tunnelling.

Two monitoring applications are studied experimentally. The first concerns load identification in fibre-reinforced shotcrete tunnel linings. Laboratory specimens were instrumented with DOFS and subjected to two load types: idealised loose rock block loads and distributed loads combined with bond loss between substrate and concrete. The results show that these load types can be distinguished from distributed strain and curvature responses before peak load is reached, demonstrating the potential of DOFS for early warning and targeted maintenance.

The second application concerns deformation monitoring in the surrounding rock mass. A DOFS-based shape sensing system was developed, evaluated in laboratory tests, and installed in a borehole adjacent to an active drill-and-blast tunnel excavation. A beam theory-based analysis method was developed to determine load direction, longitudinal deformation, and lateral deformation, including both bending and shear deformation. Laboratory results showed good agreement with reference measurements, while the field test demonstrated that the sensor can capture relative deformation in a hard rock mass.

The thesis shows that DOFS can provide spatially continuous information that improves the interpretation of local load and deformation mechanisms in underground infrastructure. This information can support safer and more efficient excavation by enabling earlier identification of unfavourable structural behaviour, more targeted inspections, and improved assessment of support performance.

Keywords: Distributed optical fibre sensors, Underground infrastructure monitoring, Shotcrete tunnel linings, Rock mass deformation.

The DOFS don't lie.

List of Publications

This thesis is based on the following publications:

[A] **August Jansson**, Ignasi Fernandez, Carlos Gil Berrocal, Rasmus Rempling, "Investigation of the Impact of Concrete Surface Treatment Methods on the Interfacial Bond Strength". *International RILEM Conference on Synergising Expertise towards Sustainability and Robustness of Cement-based Materials and Concrete Structures*, Vol. 43, 2023, pp. 925–934. doi:10.1007/978-3-031-33211-183.

[B] **August Jansson**, Ignasi Fernandez, Carlos Gil Berrocal, Rasmus Rempling, "Experimental dataset for loads on hard rock shotcrete tunnel linings in a laboratory environment". *Data in Brief*, vol. 57, no 110920, 2024.

[C] **August Jansson**, Andreas Sjölander, Ignasi Fernandez, Carlos Gil Berrocal, Rasmus Rempling, "Experimental investigation on prevalent local failure mechanisms in hard rock tunnel linings using distributed optical fibre sensors". *Engineering Structures*, vol. 333, no 120185, 2025.

[D] **August Jansson**, Ignasi Fernandez, Carlos Gil Berrocal, Rasmus Rempling, "Strain distributions for shotcrete failure in hard rock tunnels". *IABSE Symposium Manchester*, vol. 1, pp. 806–813, 2024.

[E] **August Jansson**, Carlos Gil Berrocal, Rasmus Rempling, Ignasi Fernandez, "Comparative analysis between Distributed Optic Fibre Sensors for the measurement of localised shear deformations". *Manuscript submitted to Materials and Structures.*

[F] **August Jansson**, Carlos Gil Berrocal, Rasmus Rempling, Ignasi Fernandez, "Quantification of shear deformation in discontinuity planes using distributed optical fibre sensors". *Submitted in Rock Mechanics and Geotechnical Engineering for 2^{nd} review.*

Other publications by the author, not included in this thesis, are:

A. Jansson, I. Fernandez, C.G. Berrocal, R. Rempling, "Experimental design for shotcrete tunnel lining with distributed optical fibre monitoring". *Proc. Nordic Concrete Research Symposium*, Stockholm, Aug. 2022.

A. Jansson, C.G. Berrocal, R. Rempling, I. Fernandez, "Detecting and quantifying shear fault displacements during tunnelling in hard rock using distributed optical fibre sensors". *Proc. Bergdagarna*, Gothenburg, 2025.

A. Jansson, C.G. Berrocal, R. Rempling, I. Fernandez, "Monitoring of shear deformations in hard rock discontinuities using distributed optical fibre sensors". *Tunnelling into a Sustainable Future – Methods and Technologies, Proc. of the ITA-AITES World Tunnel Congress 2025*, Stockholm.

In addition to the research presented in this thesis, the author has also co-founded a start-up company developing distributed fiber optic sensing solutions for monitoring civil engineering structures, with the aim of transferring research into practical applications.

Summary of included papers and author contribution

This chapter provides a summary of the included papers.

Paper A

Summary: The paper investigates how concrete surface treatment methods affect the interfacial bond strength between two separately cast concrete layers. The study supports the experiments conducted in Paper [B], [C] and [D], where controlled bond conditions were needed to simulate different interface behaviours. Laboratory tests compared jackhammering, grinding, grinding with sand, and grinding with free water. Jackhammered surfaces produced the highest measured bond strength, while ground surfaces resulted in low but non-zero bond strength. Adding sand had no significant effect, whereas free water slightly increased the bond strength.

Author's contribution: AJ contributed with conceptualization, methodology, implementation of experiments, analysis, visualization, writing - original draft. IF contributed with conceptualization, methodology, supervision, funding acquisition, project administration and writing – review and editing. CGB contributed with conceptualization, methodology, supervision, and writing – review and editing. RR contributed with conceptualization, methodology, supervision, funding acquisition, project administration writing - review

and editing.

Paper B

Summary: This paper presents a dataset obtained from an experimental campaign designed to simulate loads acting on shotcrete tunnel linings. The paper provides a detailed description of the experimental methodology, in which laboratory specimens were used to represent two loading conditions: loose rock block loading and distributed loading combined with loss of bond. The specimens were monitored using distributed optical fibre sensors, digital image correlation, load and pressure measurements, LVDTs, and 3D scanning. The results and discussion from the experimental campaign are presented in Papers [C] and [D].

Author's contribution: AJ contributed with conceptualization, methodology, implementation of experiments, writing - original draft. IF contributed with conceptualization, methodology, supervision, funding acquisition, project administration and writing – review and editing. CGB contributed with conceptualization, methodology, supervision, and writing – review and editing. RR contributed with conceptualization, methodology, supervision, funding acquisition, project administration writing - review and editing.

Paper C

Summary: The paper investigates the use of DOFS to identify local load conditions prior to failure in fibre-reinforced shotcrete tunnel linings. Laboratory specimens were designed to represent hard rock tunnel linings subjected to two common load cases: a loose rock block and distributed loose rock material. The results showed that DOFS can distinguish between these load conditions through characteristic strain patterns. Furthermore, the results showed that lining thickness strongly influenced peak load capacity, while substrate roughness affected strain distribution under bending.

Author's contribution: AJ contributed with conceptualization, methodology, implementation of experiments, writing - original draft. AS contributed with conceptualization, analysis, writing - original draft. IF contributed with conceptualization, methodology, supervision, funding acquisition, project administration and writing – review and editing. CGB contributed with concep-

tualization, methodology, supervision, and writing – review and editing. RR contributed with conceptualization, methodology, supervision, funding acquisition, project administration writing - review and editing.

Paper D

Summary: This paper investigates strain distributions in fibre-reinforced concrete specimens representing shotcrete tunnel linings in hard rock after reaching the maximum load. Distributed optical fibre sensors were embedded in laboratory specimens subjected to two loading conditions: a loose rock block and distributed loose rock material. The study examined the effects of loading condition, load size, lining thickness, and substrate surface treatment. Curvature calculated from distributed strain measurements enabled detection of load-induced bond loss. Hydro-demolished, rougher interfaces produced more progressive delamination and greater post-peak ductility, while ground interfaces showed more abrupt failure and reduced residual load-bearing capacity.

Author's contribution: AJ contributed with conceptualization, methodology, implementation of experiments, writing - original draft. IF contributed with conceptualization, methodology, supervision, funding acquisition, project administration and writing – review and editing. CGB contributed with conceptualization, methodology, supervision, and writing – review and editing. RR contributed with conceptualization, methodology, supervision, funding acquisition, project administration writing - review and editing.

Paper E

Summary: This paper compares two distributed optical fibre cable types for measuring localised shear deformation in a shape sensing system based on DOFS. A robust multilayer BRUsens V9 cable and a thinner acrylic-coated fibre were bonded to the same aluminium rod and tested in a concrete specimen with predefined shear planes. The acrylic-coated fibre captured sharper local strain peaks and was more sensitive to small strain variations, but it was also more prone to strain artefacts, data loss, and likely debonding under increasing deformation. The V9 cable produced smoother, more stable strain profiles and more reliable curvature and displacement estimates over larger

deformation ranges.

Author's contribution: AJ contributed with conceptualization, methodology, implementation of experiments, writing - original draft. CGB contributed with conceptualization, methodology, supervision, and writing – review and editing. RR contributed with conceptualization, methodology, supervision, funding acquisition, project administration writing - review and editing. IF contributed with conceptualization, methodology, supervision, funding acquisition, project administration and writing – review and editing.

Paper F

Summary: This paper presents a method for quantifying shear deformation in discontinuity planes, such as rock joints, using distributed optical fibre sensors mounted along beam-like elements. Based on Timoshenko-Ehrenfest beam theory, the method separates bending, shear, and longitudinal deformation from measured strain data and identifies shear zones using curvature gradients. Two laboratory experiments with shape sensing systems embedded in concrete specimens were used for validation. The results showed good agreement between calculated deformations, direct displacement measurements, and post-test 3D scans. Although promising, the method requires further field validation to address scale effects, rock stiffness, joint gaps, and sensor orientation.

Author's contribution: AJ contributed with conceptualization, methodology, implementation of experiments, writing - original draft. CGB contributed with conceptualization, methodology, supervision, and writing – review and editing. RR contributed with conceptualization, methodology, supervision, funding acquisition, project administration writing - review and editing. IF contributed with conceptualization, methodology, supervision, funding acquisition, project administration and writing – review and editing.

Contents

Abstract ii

List of Papers vii

Acknowledgements xvii

I Extended Summary 1

1 Introduction 3
- 1.1 Background . . . 3
- 1.2 Purpose and objectives . . . 4
- 1.3 Scientific approach . . . 5
- 1.4 Scope and limitations . . . 6
- 1.5 Thesis outline . . . 7

2 Frame of reference 9
- 2.1 Load and deformation in hard rock during tunnel construction 9
- 2.2 Conventional monitoring and inspection of tunnels in hard rock 11
- 2.3 Distributed optical fibre sensors . . . 13
- 2.4 Monitoring of structures, soil and rock using DOFS . . . 14

3 Laboratory experiments **17**
3.1 Shotcrete lining experiments 17
3.2 Shape sensor experiments 20

4 Field test **23**
4.1 Site 23
4.2 Sensor preparation 25
4.3 Installation 25
4.4 Measurements 27

5 Data Analysis **29**
5.1 Shotcrete linings 29
5.2 Shape sensor 30
Load direction 31
Bending deformation 32
Shear and longitudinal deformation 33

6 Results **37**
6.1 Lab experiments 37
Shotcrete experiments 37
Shape sensor experiments 40
6.2 Field test 45
Deformation during blasting 46
Full monitoring scheme 51

7 Discussion **57**
7.1 Rock substitutes and laboratory limitations 57
7.2 Shotcrete linings 58
7.3 Shape sensor prototyping 59
7.4 Shape sensor field applicability 61

8 Conclusions and Future Work **63**
8.1 Conclusions 63
8.2 Future work 66

References **69**

II Papers **77**

A Paper A **A1**

B Paper B **B1**

C Paper C **C1**

D Paper D **D1**

E Paper E **E1**

F Paper F **F1**

Acknowledgments

The work presented in this thesis was carried out at the department of architecture and civil engineering at Chalmers University of Technology between 2022 and 2026. I would like to extend my sincere gratitude to the funders of this research, the Swedish transport administration through BBT and BeFo with grant number 2020-006 and 532, respectively.

I am thankful to my supervisors, Associate Professor Ignasi Fernandez, Dr. Carlos G. Berrocal, and Associate Professor Rasmus Rempling, for challenging me to develop as a researcher. I am grateful for all the advice you gave, even though I did not always follow it. I would also like to thank the lab engineers, Sebastian Almfeldt, Anders Karlsson and Bruno Gonçalves for making my experimental designs work. Your practical insights and solutions to my problems have been extremely valuable. Further, I would like to thank all my colleagues in the division, especially those sharing an office with me, for creating a fun and enjoyable working environment.

The field test in this thesis would not have been possible without John Eliasson and Gay Plato. Thank you for facilitating the field test and for assisting me in completing the project.

Finally, I would like to thank my wife Jennifer for her love and support throughout this process. This journey would not have been possible without having you by my side.

Declaration of generative AI in scientific writing

During the preparation of this work, the authors used Microsoft Copilot in order to improve the readability and language of this thesis. After using this tool, the authors reviewed and edited the content as needed and take full responsibility for the content of the publication.

Part I

Extended Summary

CHAPTER 1

Introduction

1.1 Background

Tunnelling and underground construction have become progressively safer and more efficient through advances in construction methods, equipment, support systems, design approaches, and monitoring techniques. Monitoring is commonly required in underground construction projects to verify design assumptions, control the excavation process, and assess the potential impact on surrounding structures and infrastructure [1].

The type and extent of monitoring used during underground construction depend largely on the selected design approach and the complexity of the project. In more complex projects, monitoring is often applied more extensively to verify the performance of support structures and to control ground deformations around the excavation. In conventional design approaches, safe and reliable designs are typically achieved by applying partial factors in the design for load-bearing structures, which reduces the need for design verification through monitoring [2]. In contrast, when the observational method is used, monitoring plays a central role by providing information during construction that can be used to update the design and adjust construction measures as

needed to maintain safety and reliability [3].

Conventional monitoring methods typically measure structural response at discrete points or surfaces [4], [5]. As a result, the behaviour between measurement locations must be inferred or interpolated. This can be insufficient when the structural response is complex, for example in anisotropic materials such as jointed rock masses, where deformation and load transfer may occur along discrete discontinuity planes. Limited spatial coverage can therefore make it difficult to identify local effects, load redistribution, and non-uniform structural behaviour.

Distributed optical fibre sensors (DOFS) offer a means to improve this information basis [6]. By providing distributed strain measurements along an optical fibre, DOFS can capture local variations in structural response that may not be detected by point-based monitoring systems. This enables a more detailed evaluation of the behaviour of tunnels and underground support systems, and can improve the interpretation of measurements. In this way, DOFS have the potential to support more reliable design assumptions and contribute to safer and more efficient tunnelling processes.

1.2 Purpose and objectives

The purpose of this work is to advance the monitoring processes during construction of underground infrastructure. The work has focused on developing methods for identifying load types induced in tunnel linings and measuring deformations in the surrounding rock during tunnel excavations. The purpose of this thesis is further defined by the following objectives:

1. To identify load types acting on shotcrete tunnel linings in rock tunnels using DOFS.
2. To demonstrate the adequacy of advanced sensor-based monitoring systems for obtaining unique and trustworthy data in shotcrete tunnel linings.
3. To devise a DOFS-based sensing system suitable for measuring deformations in rock induced by tunnel excavation.
4. To develop a method for detecting, locating, and quantifying shear deformations utilising longitudinal strains measured in the sensing system.

1.3 Scientific approach

The objectives are experimentally addressed through two underground infrastructure applications: the interface between the tunnel and the surrounding rock mass, i.e., shotcrete linings, and the local deformation of rock masses at discontinuity planes. A first experimental campaign (Objectives 1 and 2) investigates load types and deformations occurring in shotcrete tunnel linings. A second campaign (Objectives 3 and 4) investigates deformations in discontinuity planes induced by tunnel excavations. The developed sensor system, hereafter referred to as the shape sensor, and the analysis methods were further assessed through a field test, with the aim of evaluating their applicability and accuracy under in situ conditions. In Figure 1.1, the workflow of the project and the relation between the included papers and the field test described in Chapter 4 are presented.

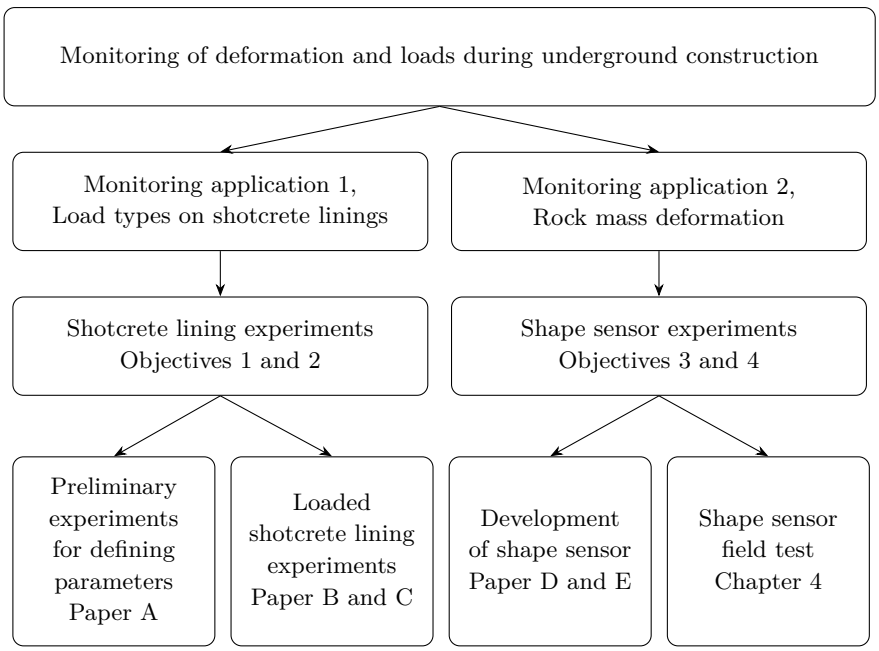


Figure 1.1: Overview and structure of the work presented in this thesis.

The work presented in this thesis combines experimental, analytical, and

data-driven methods to address the stated research objectives. These methods are applied in combination, where laboratory testing provides controlled conditions for evaluating the monitoring applications, and structural analysis and data processing support the interpretation of the measured response.

In Paper [A], preliminary experiments were conducted aimed at characterizing bond properties between a shotcrete layer and a concrete slab for the experiments presented in Papers [B], [C] and [D]. The experiments presented in Papers [B]–[F] were exploratory in nature, although different strategies were used. In Papers [B], [C] and [D], a full factorial design with one repetition was used to systematically investigate the influence of selected parameters on the response of DOFS-instrumented shotcrete lining specimens. In Papers [E] and [F], an iterative prototyping and testing approach was adopted to develop and evaluate the shape sensor concept and associated analysis methods.

1.4 Scope and limitations

The scope of this thesis is limited to applications in hard rock using distributed optical fibre sensors (DOFS). The work specifically considers DOFS systems based on optical frequency-domain reflectometry (OFDR) and Rayleigh backscattering, which enable spatially distributed strain measurements with high spatial resolution. Other monitoring techniques, sensing principles, or instrumentation strategies are used for verification and to contextualise the selected fibre-optic approach.

For the monitoring application in shotcrete linings, the work is restricted to two selected load cases, a loose rock block acting on the lining and a distributed load acting on the lining, representing idealised loading conditions relevant to hard rock tunnel linings. Other possible actions and influences, including tunnel convergence, environmental effects, time-dependent behaviour, and long-term loading, are not included in the present investigation.

For the shape sensor application and the developed model for determining shear deformation in discontinuities, only perpendicular discontinuity planes are considered. Furthermore, only the deformation induced during the excavation process of a tunnel lining is studied, whereas the long-term deformation development, degradation mechanisms, and changes occurring during the operational phase are not considered within this application.

The experimental work in this thesis was primarily conducted under labora-

tory conditions, which limited the extent to which in situ hard rock conditions could be reproduced. First, the size of the specimens was constrained by the capacity of the laboratory setup, resulting in a scale difference between the experiments and field conditions. Second, the stress-strain state representative of in situ hard rock could not be reproduced in the laboratory, as the specimens could not be subjected to the same confinement, boundary conditions, or stress history as rock mass in the field would be.

The field test was carried out during an active tunnel excavation project, which imposed additional practical limitations. As the work had to be adapted to the ongoing construction process, there was limited control over the blasting sequence, sensor placement, and access to the installed sensor.

1.5 Thesis outline

This thesis consists of 8 chapters and 6 appended papers. The content of the included chapters is summarised below.

Chapter 1 – Introduction Describes the background, purpose, scientific approach, scope, and limitations of the thesis.

Chapter 2 – Frame of reference Presents the theoretical background and relevant literature.

Chapter 3 – Laboratory experiments Summarises the experiments conducted in the appended papers.

Chapter 4 – Field test Describes the site, installation, and measurement scheme for the conducted field test.

Chapter 5 – Data analysis Presents the analysis methods applied to the experimental data.

Chapter 6 – Results Summarises the laboratory results included in the appended papers and presents unpublished results for the field test.

Chapter 7 – Discussion The results are discussed concerning the limitations of the experiments, applicability of the monitoring applications in the field, and prototyping of the shape sensor.

Chapter 8 – Conclusions and future work Presents conclusions and recommendations for future research.

CHAPTER 2

Frame of reference

In this chapter, research relevant to the work conducted in this thesis is reviewed.

2.1 Load and deformation in hard rock during tunnel construction

As tunnels and underground spaces are excavated, the initial stress-strain state of the surrounding rock mass is disturbed. Deformation develops as the rock mass redistributes stresses and reaches a new equilibrium around the excavated volume. This process also changes the load distribution in the rock mass. Loads that were previously carried by the excavated volume are transferred to the tunnel boundary through arching action in the rock mass above the tunnel roof [7].

The magnitude and distribution of the resulting deformation and load depend on the properties of the rock mass, including stiffness, strength, and geometry and density of joints. Rock joints introduce anisotropy into the rock mass, which makes the deformation response non-uniform and difficult

to predict. Deformation may occur both within the intact rock and along discontinuities, and the relative contribution of these mechanisms depends on the local geological and mechanical conditions.[8]

Rock mass deformation may occur both as continuous deformation of the intact rock matrix and as localised shear displacement along pre-existing discontinuities such as rock joints. Shear displacement along a natural rock joint is generally accompanied by dilation, i.e. an opening normal to the joint plane. This occurs because rock joint surfaces are rough and irregular. When the two joint surfaces are sheared relative to one another, the opposing asperities interlock and resist sliding. Continued shear displacement, therefore, requires the surfaces to move over these asperities, which induces a displacement component normal to the joint plane. The amount of dilation depends on factors such as joint roughness, normal stress, infilling, and the degree of mechanical interlocking. [7]

Additionally, the deformations induced by excavation can remove the confinement and support that previously acted on the rock around the tunnel perimeter. In a jointed rock mass, this may leave blocks defined by intersecting discontinuities partly or completely unsupported. Their stability depends on the joint geometry and properties, as well as on the confinement and mechanical interlocking provided by the surrounding rock mass. If the resisting forces are insufficient, the block will detach and fall into the excavation. [9]

In hard rock tunnels, the most common support system consists of rock bolts and a shotcrete lining. The primary purpose of this system is to stabilise potentially loose blocks around the tunnel perimeter and prevent rock fallout. By keeping these blocks in place, the support system helps maintain contact and mechanical interlocking within the surrounding rock mass. This allows the rock mass to continue contributing to load redistribution around the excavation, while the support system provides local reinforcement and surface retention where the natural stability of the jointed rock mass is insufficient. [10], [11], [12]

These support systems are designed through empirical, analytical and numerical methods. The numerical methods are typically reserved for more complex tunnel geometries, whereas the analytical methods use conservative assumptions for loads as exact rock joint geometries cannot be established before blasting [13]. The empirical methods apply rock classifying systems based on properties of the rock and rock joints [14], [15]. From the classification of

the rock and the tunnel geometry, the support system is designed based on previous experience.

2.2 Conventional monitoring and inspection of tunnels in hard rock

During tunnel construction, monitoring the response of the rock mass and support structures is essential for verifying design assumptions and maintaining safe, controlled excavation procedures [1], [14]. The required extent of monitoring depends on project-specific conditions and the associated risk management strategy. In rural tunnel excavations or mining environments, larger deformations may be more acceptable than in urban excavations, where deformations can pose larger risks to third parties. Similarly, in automated mining operations with limited human presence, a higher tolerance for risk pertaining to local rock fall-out or collapse may be accepted compared to an urban excavation.

The two monitoring applications investigated in this thesis are primarily relevant to projects where a high level of deformation control is required and where monitoring is used to reduce risk. In the first monitoring application, which concerns loads acting on shotcrete linings, conventional assessment relies mainly on visual inspection. Before shotcrete is applied, the exposed rock surface is inspected and mapped to identify joint geometries, rock mass quality, and potentially unstable blocks. After the shotcrete has been applied, and throughout the service life of the support system, inspection is typically performed visually, sometimes supported by techniques such as LiDAR scanning [16]. Hammer sounding may also be used to identify areas where bond loss or delamination has occurred between the shotcrete lining and the rock surface.[17]

For the second monitoring application, which concerns deformation in the rock mass and along rock discontinuities, existing methods for measuring such deformation include surveying using total stations, extensometers, and inclinometers [4]. These techniques can be used to monitor changes in tunnel geometry, such as convergence, as well as surface settlements above the tunnel and deformations within the surrounding rock mass . However, they generally provide measurements at discrete locations and often measure the deformation response indirectly. As a result, assumptions and interpolation are required to

interpret the deformation mechanisms occurring within the rock mass. Distributed or semi-distributed monitoring techniques can reduce the need for such assumptions and interpolation by providing a more continuous representation of the response of the monitored rock mass or support structure.

Several techniques have been developed for measuring rock mass deformation more directly and with improved spatial coverage. These include shape accelerometer arrays (SAA), probing or concatenated inclinometers, time domain reflectometry (TDR), and Fibre Bragg grating (FBG) sensors connected in series.

SAA systems consist of arrays of accelerometers connected in series, from which displacements can be obtained in three directions at discrete locations along the array [18]. Similarly, probing and concatenated inclinometers can be used to monitor inclination along a borehole, allowing deformation of the bore hole to be evaluated.

In TDR, a cable is installed in a borehole and probed using an electrical pulse. Reflections along the cable are then measured, and increases in the reflected signal can indicate locations where the cable has been deformed or damaged [19]. In FBG-based systems, a laser pulse is transmitted through an optical fibre containing Bragg gratings. Each grating reflects a specific wavelength, and deformation of the grating causes a shift in the reflected wavelength that can be related to strain [20]. By connecting several FBG sensors in series and analysing the response through multiplexing, quasi-distributed sensing systems can be created.

These techniques are useful for measuring large or distributed deformation along a borehole, but they are less suited for localised deformation, such as shear displacement along individual rock joints. SAA and inclinometer systems lack the spatial resolution needed to resolve such localised deformation, while TDR generally indicates shear-induced cable damage only after the deformation has become sufficiently large. FBG sensors provide high-sensitivity strain measurements, but the number of gratings that can be connected in series is limited. Consequently, the position of the relevant rock joint or active shear plane must often be known before installation if the sensors are to be placed where localised shear deformation is expected.

2.3 Distributed optical fibre sensors

As described in Chapter 1, this thesis investigates the implementation of DOFS for monitoring rock deformation and loads acting on shotcrete tunnel linings. The use of DOFS is intended to provide distributed measurements with high spatial resolution and to enable more direct interpretation of load and deformation mechanisms in underground infrastructure.

A DOFS system consists of an optical fibre connected to an interrogator, which, in simplified terms, comprises a laser source and a photodetector. The interrogator sends light into the fibre, and the photodetector records the signal that is backscattered from the fibre. By analysing variations in this backscattered signal, strain and temperature changes can be determined along the length of the optical fibre.

The backscattered signal in optical fibres consists of Raman, Brillouin, and Rayleigh scattering components. Raman backscattering is primarily sensitive to temperature, whereas Brillouin backscattering is affected by both temperature and strain. Rayleigh backscattering is also influenced by changes in both temperature and strain and can be analysed using optical frequency domain reflectometry (OFDR). [21], [22]

In this thesis, Rayleigh-based OFDR was used because it provides substantially higher spatial resolution than sensing techniques based on Brillouin backscattering. The system used in this work has a minimum gauge length of 0.65 mm, which enables localised strain variations to be resolved. This high resolution is particularly important for detecting local deformation mechanisms such as concrete cracking [23], [24], or shear deformation along discontinuities [25], [26]. A limitation of Rayleigh-based OFDR is that the maximum sensing length is shorter than for Brillouin-based systems. The OFDR system used for this work can measure over distances of up to 100 m, whereas Brillouin-based systems can reach lengths on the order of kilometres [21]. For both techniques, however, increasing the measurement range generally reduces the achievable spatial resolution.

2.4 Monitoring of structures, soil and rock using DOFS

DOFS technology has been applied across several areas of civil engineering research. In structural engineering, DOFS have been used in reinforced concrete structures to monitor cracking through strain variations measured in loaded laboratory specimens [23], [27], [28], [29], [30]. When installed in beams, the distributed strain measurements can also be combined with beam theory to evaluate crack widths and structural deformations [24], [31], [32], [33]. Beyond laboratory studies, DOFS have been implemented in field applications for structural health monitoring, demonstrating their potential for capturing distributed strain responses in real structures [34], [35], [36], [37], [38].

DOFS have also been used in several geotechnical monitoring applications. In pile foundations, DOFS have been installed to investigate load transfer and deformation interaction between piles and the surrounding ground [39], [40], [41]. Such instrumented piles are conceptually similar to the shape sensor application presented in this thesis, as the DOFS are installed along a beam-like element and used to interpret its deformation. Similar approaches have also been applied to beam-like elements in soil, where beam theory has been used to derive deformation from measured strain distributions [42], [43], [44], [45], as well as to instrumented rock bolts [26], [46], [47]. These sensor designs and analysis methods can capture longitudinal and bending deformation, but they are generally not suitable for identifying or quantifying localised shear deformation, as discussed in [48].

In tunnelling applications, DOFS have been used both to monitor the response of surrounding structures during excavation [49], [50], [51] and to measure deformation developing within tunnels during construction [52], [53], [54], [55], [56]. In [54] and [56], DOFS were installed in shotcrete linings to monitor tunnel convergence, deformation, and strain variations during excavation. However, these studies did not investigate load mechanisms associated with loose rock blocks or loss of bond between the shotcrete lining and the surrounding rock mass.

Despite the significant developments in structural and geotechnical monitoring through DOFS, there remains a need for monitoring approaches capable of identifying load mechanisms in shotcrete tunnel support systems and quantifying localised shear deformation in jointed rock masses. These research gaps

form the basis for the work presented in this thesis.

CHAPTER 3

Laboratory experiments

This chapter presents the experimental work conducted in this thesis. The first part describes the monitoring application related to shotcrete linings, while the second part addresses the experiments associated with the development and evaluation of the shape sensor.

3.1 Shotcrete lining experiments

To investigate monitoring application 1, as described in Chapter 1, an experimental campaign was designed. The specimens consisted of a 300 mm thick concrete substrate slab, representing the rock, and a cast fibre-reinforced concrete top layer, representing fibre-reinforced shotcrete. A full factorial design was implemented with four parameters, each considered at two levels, resulting in 16 unique specimens. The investigated parameters were load case, loaded area size, top layer thickness, and surface treatment of the substrate slab before casting the top layer. These parameters were varied to generate different load and failure mechanisms in the specimens. Table 3.1 presents the factorial design, including the factors, levels, and nomenclature used for each specimen, and in Figure 3.1 the experimental setup is shown.

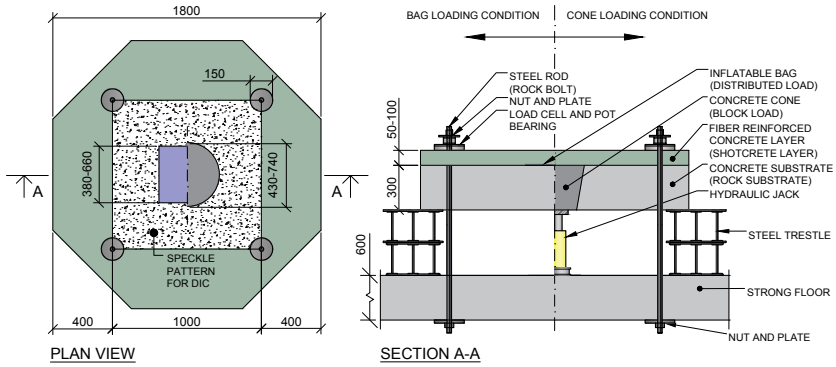


Figure 3.1: Experimental setup for simulating loads on shotcrete linings. The left side in both figures shows the lifting bag load case and the right side shows the cone loading load case. Adapted from Paper [B].

Table 3.1: Factorial design for the shotcrete experiments. Each specimen name is an abbreviation of the included factor levels, with the corresponding letter or number underlined in the table.

						Surface treatment	
						Hydro	Ground
Load condition	Cone	Loading area	Small	Top layer thickness [mm]	50	CS50H	CS50G
					100	CS100H	CS100G
			Large		50	CL50H	CL50G
					100	CL100H	CL100G
	Lifting Bag		Small		50	BS50H	BS50G
					100	BS100H	BS100G
			Large		50	BL50H	BL50G
					100	BL100H	BL100G

The two load cases used in the experiments were intended to represent a loose rock block acting on a shotcrete lining and a loss of bond between the rock and shotcrete layer combined with a distributed load from loose rock material. To simulate a loose block acting on the shotcrete lining, a cone-shaped loading body was cast in the centre of the concrete substrate slab. Steel sheet formwork was used to separate the cone from the surrounding substrate concrete which was removed after hardening. The wide end of the cone was positioned at the top of the substrate slab, and the narrow end at the bottom. During loading, a hydraulic jack installed below the specimen pushed against the narrow end of the cone. The cone geometry was selected instead of, for example, a cylindrical loading body, to minimise friction between the loading body and the surrounding substrate slab.

The load case representing loss of bond combined with loose rock material was simulated by installing an inflatable square lifting bag between the substrate slab and the top layer. During casting of the top layer, the lifting bag was covered with a plastic sheet to prevent bonding between the bag and top concrete layer in the loaded area. During loading, the bag was filled with hydraulic oil, thereby applying a distributed load to the top layer simulating loose rock material acting on the shotcrete lining.

The surface treatment parameter was included to create different bond conditions between the substrate slab and the top layer, representing high and low bond strength. Preliminary experiments were conducted to evaluate methods for producing these bond conditions, as presented in Paper [A]. Four surface preparation methods were investigated. The results showed that grinding the substrate slab before casting the top layer produced a low bond strength, whereas jackhammering the substrate surface before casting resulted in a high bond strength.

For the main experimental campaign, grinding was selected for specimens representing low bond strength, while hydro-demolition was selected for specimens representing high bond strength. Hydro-demolition produces a surface roughness similar to that obtained by jackhammering, but induces fewer and smaller microcracks in the near-surface concrete, which could otherwise reduce the bond strength between the layers [57]. It was also selected because it is less labour-intensive than jackhammering.

The thickness of the top layer was set to either 50 mm or 100 mm to simulate a thin and a thick concrete layer. For a hard rock tunnel lining,

shotcrete thickness is usually chosen between 50 mm and 150 mm [58]. For the cone-loaded specimens, the loaded wider diameter of the cone was either ϕ430 mm or ϕ740 mm, while for the bag-loaded specimens the loaded area was either 380 mm × 380 mm or 660 mm × 660 mm. DOFS were installed in the top layer at two levels: one sensor layer was positioned 10 mm below the top surface, and the other 10 mm above the interface between the top layer and the substrate slab. At each level, fibre optic cables were installed in two orthogonal directions.

3.2 Shape sensor experiments

For the second monitoring application, experiments were designed to reproduce shear deformation along discontinuities in a rock mass and to evaluate a sensor system developed to measure this deformation. The sensor system, referred to as a shape sensor, consists of a sensor guide instrumented with three or more DOFS bonded longitudinally along its surface. The sensor guide is a beam-like element with elastic or elastic-plastic material behaviour, such as the aluminium rods and tubes used in Papers [E] and [F].

To simulate shear deformation along a rock discontinuity, two different experimental setups were designed. In the first setup, a concrete block was cast and a cylindrical core was drilled out from the block. The cylinder was then reinserted into the block and pushed through it to induce shear deformation between the cylinder and the surrounding concrete. A shape sensor was installed perpendicular to the cylinder to measure the resulting deformation. In this specimen, the shape sensor consisted of three 0.9 mm nylon-coated optical fibre cables bonded to a 40 mm diameter aluminium tube with 3 mm wall thickness using 3M Scotch-Weld DP190 epoxy as presented in Figure 3.4a. The displacement of the loading cylinder relative to the surrounding concrete block was measured using three LVDTs mounted on the cylinder, equally spaced at 120°. The specimen is shown in Figure 3.2.

The second experimental setup consisted of three separately cast concrete blocks placed in line. A shape sensor was installed through all three blocks. To induce load, a hydraulic jack was installed above the middle block to apply a downward load perpendicular to the shape sensor, while the outer blocks were supported by steel trestles. The experimental setup is shown in Figure 3.3. This loading arrangement induced shear deformation between the middle

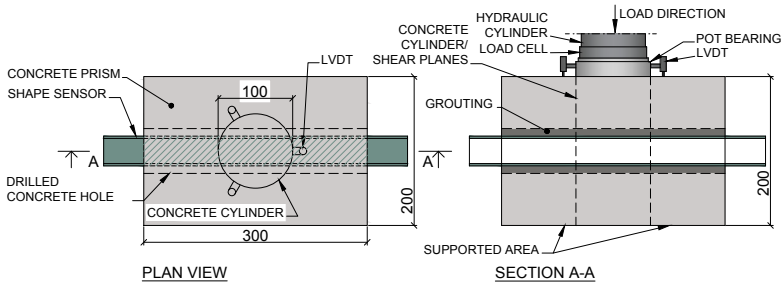


Figure 3.2: Experimental setup for the first shape sensor experiment. Adapted from Paper [F].

block and the two outer blocks. The displacement of the middle block relative to the outer blocks was measured using digital image correlation (DIC) on the long side of the specimen. In this specimen, the shape sensor consisted of a 40 mm diameter aluminium rod instrumented with four 3.2 mm BRUSens V9 cables and four 0.25 mm acrylic-coated optical fibre cables as shown in Figure 3.4b. The optical cables were glued to the aluminium rod using 3M Scotch-Weld DP190.

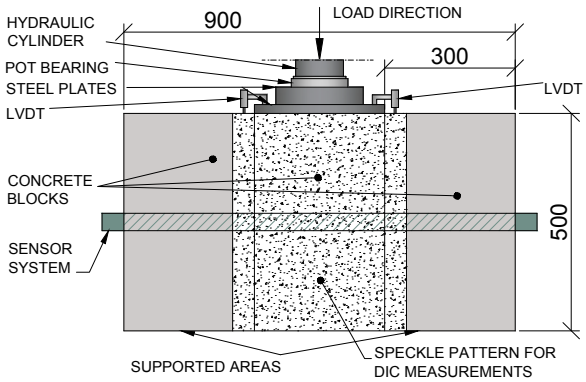


Figure 3.3: Experimental setup for the second shape sensor experiment. Adapted from Paper [F].

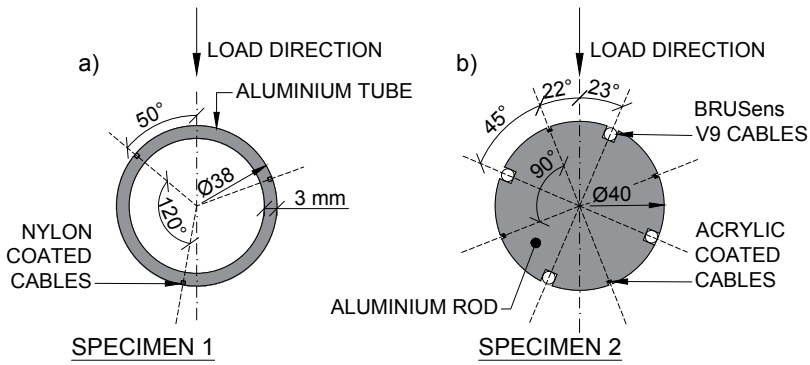


Figure 3.4: Shape sensor cross sections for a) the first specimen and b) the second specimen.

CHAPTER 4

Field test

This chapter presents unpublished work from a field test in which a shape sensor was installed in the rock mass adjacent to a planned tunnel excavation and monitored during excavation. The purpose of the test was to investigate whether the sensor could capture excavation-induced deformation during an ongoing drill-and-blast tunnelling project.

4.1 Site

The field test was conducted during an ongoing tunnel excavation project in central Gothenburg. The monitored tunnel was accessed through a 200 m long service tunnel and was excavated using the drill-and-blast method. Excavation proceeded in both directions from the point where the service tunnel connected to the main tunnel. The monitored tunnel section was approximately 15 m wide, with an overburden of about 25 m above the tunnel crown. A plan view of the site is shown in Figure 4.1a, while Figure 4.1b presents an elevation of the tunnel under construction.

The excavation sequence is also indicated in Figure 4.1. The excavated rock volume is shown in orange and labelled with dates corresponding to

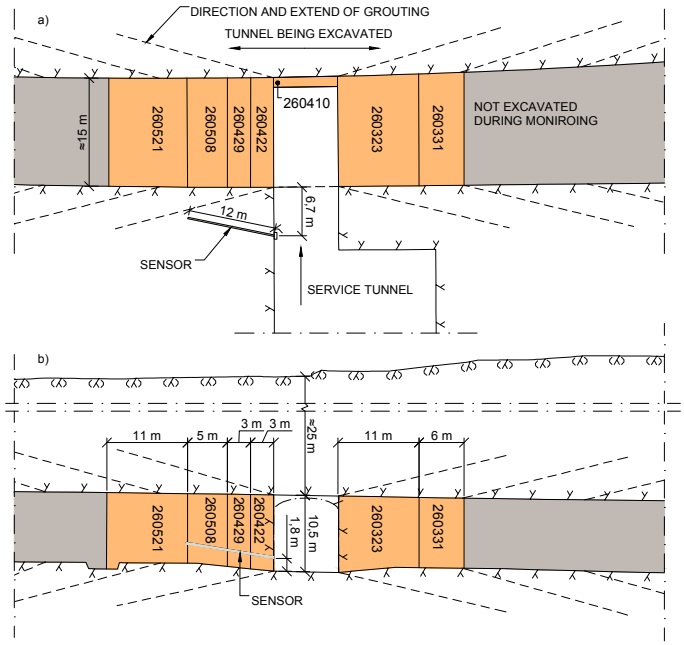


Figure 4.1: a) Plan view of the tunnel under consideration, the connecting service tunnel and the sensor position. b) Elevation of the tunnel under consideration and vertical position of the sensor. The parts excavated during monitoring are coloured in orange and the dates indicate the extent of excavation at each monitoring occasion.

the extent of excavation at each measurement occasion. These dates indicate, therefore, both the progression of the excavation and the times at which sensor measurements were obtained.

The rock mass at the site consists mainly of granodiorite gneiss with a uniaxial compressive strength (UCS) ranging from 100 to 250 MPa. According to the rock mass mapping protocol, the rock quality designation (RQD) in the vicinity of the sensor was assigned a value of 100, and the rock mass quality was generally classified as Q = 50 according to the Q-system [15]. At the intersection between the service tunnel and the main tunnel, pegmatite stringers were recorded in the service tunnel, oriented in the same direction as

the excavation direction of the main tunnel. The rock mass quality associated with these pegmatite stringers was lower, with a calculated Q-value of 9.

4.2 Sensor preparation

The shape sensor used in the field test consisted of a 40 mm diamter aluminium rod that served as the sensor guide and four BRUSens DSS V9 optical fibre cables. The total length of the assembled shape sensor was 12 m. To facilitate transportation and handling before installation, the aluminium rod was divided into 1.5 m long segments that could be connected on site. Each connection was formed by drilling a hole in one end of a segment and milling down the diameter of the adjoining end so that it fitted into the drilled hole. The connected segments were then fixed together using dowels installed through the joint. A photograph of the assembled connection is presented in Figure 4.2a and a schematic of the sensor guide connection is shown in Figure 4.2b. A small gap of 5 mm, shown in Figure 4.2a, was left between adjacent aluminium rods on the perimeter of the rods to accommodate potential minor misalignment during installation.

To encapsulate the optical fibre cables and ensure that they were positioned in straight lines along the sensor guide, four 4 × 4 mm slits were sawn along the aluminium rod at 90° intervals around its circumference, as shown in Figure 4.2. After the full sensor guide had been assembled and secured with dowels, the cables were glued into the slits on site using 3M DP105 epoxy. This adhesive was selected because of its shorter curing time compared with the DP190 epoxy used in appended papers [E] and [F]. The assembled shape sensor is shown in Figure 4.3a.

4.3 Installation

The shape sensor was installed from the service tunnel in a borehole drilled alongside the monitored tunnel, as shown in Figure 4.1. This orientation was selected to enable the measurement of the deformations induced by the tunnel excavation. The borehole was 12.5 m long and had a diameter of 64 mm. After installation, the sensor was grouted in place to ensure contact with the surrounding rock mass. To reduce the risk of entrapped air during grouting, the grout was injected at the far end of the borehole through an

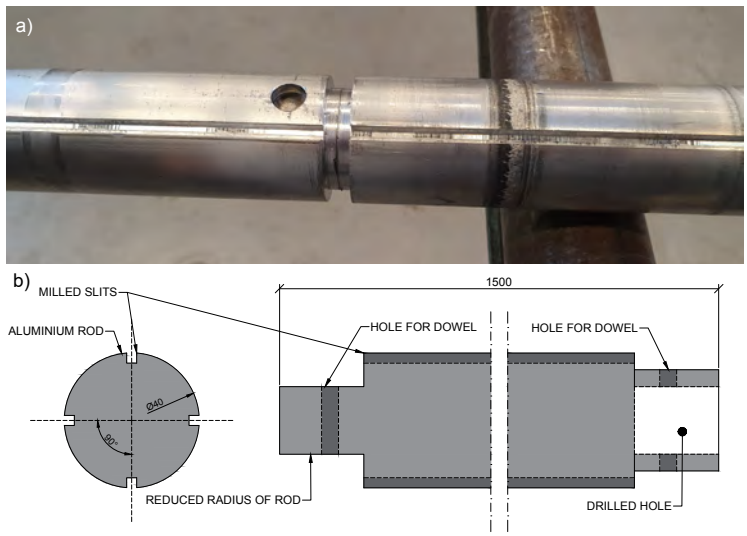


Figure 4.2: a) A picture of the connection prior to inserting the dowel and b) a schematic figure of the connection detail between aluminium rods.

18 mm diameter plastic tube. Figure 4.3b shows the sensor installed in the borehole before grouting.

To allow access to the DOFS in the shape sensor, approximately 20 cm of the sensor end was left protruding from the rock surface. An appliance box with a cut-out for the sensor was mounted on the rock to protect the fibre connections from dust that could contaminate the ferrules at the connection between the sensor cables and the interrogator system. In addition, a steel shield was installed to protect the sensor and the appliance box from debris generated during blasting. The appliance box and steel shield are shown in Figure 4.4a.

Inside the appliance box, the DOFS were connected to interrogator modules, which were in turn connected to 200 m long stand-off cables. In Figure 4.4b, the inside of the appliance box is shown. The stand-off cables were routed from the appliance box further up the service tunnel and connected to a LUNA Innovations ODiSI 6108 interrogator. Positioning the interrogator away from the excavation face protected it from blasting debris and reduced the risk to the operator by placing the measurement equipment in an area with less

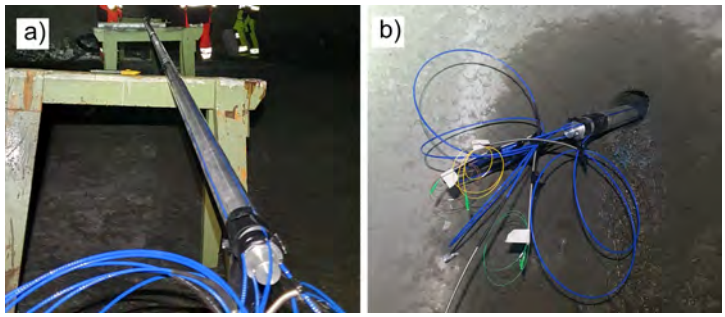


Figure 4.3: a) Assembled shape sensor prior to installation in borehole, and b) shape sensor installed in the borehole prior to grouting.

construction traffic and fewer moving machines.

4.4 Measurements

Although protective measures were implemented to reduce the risk of damage to the measurement equipment, it became clear after the first blast that these measures were not sufficient to guarantee the integrity of the system. The shock wave from blasting easily compromised the water and dust sealing of the appliance box. In addition, after one blast was detonated in the direction opposite to the sensor, the resulting debris indicated that a direct impact could potentially damage or destroy both the steel shield and the appliance box. No such direct impact occurred during the excavation, but the risk was considered significant.

To limit the exposure of the measurement equipment, the monitoring strategy was therefore changed from continuous monitoring to measurements at approximately one-week intervals during the excavation. To capture the sensor response during blasting, measurements were nevertheless performed during one blast event on 22 April 2026, when the risk of a direct hit from blasting debris was considered low.



Figure 4.4: a) Appliance box installed at the beginning of the sensor and protective shield. b) Installations in the appliance box, including the end of the shape sensor, extension modules and extension cable.

CHAPTER 5

Data Analysis

This chapter describes the analysis of the experimental data obtained from the experimental programmes presented in Chapters 3 and 4. The purpose of this chapter is to explain how the measurements were processed and interpreted to extract information relevant to the research objectives. The chapter is divided into two main parts. The first concerns the analysis of experiments related to load identification in shotcrete tunnel linings, while the second focuses on the analysis of the shape sensor.

5.1 Shotcrete linings

For the experiments simulating loads acting on shotcrete linings, the strain in the top and bottom of the top concrete layer was combined by calculating a one directional curvature along the DOFS. The one directional curvature is calculated as

$$\chi = \frac{\varepsilon_{top} - \varepsilon_{bot}}{z} \tag{5.1}$$

where ε_{top} is the strain value in the top DOFS layer, ε_{bot} is the strain value in the bottom DOFS layer, and z is the distance between the two sensor cables.

The one-directional curvature was calculated to enable comparison between specimens and to provide a parameter that could potentially be applied to strain measurements from real shotcrete linings. In field applications, both the thickness of a sprayed shotcrete lining and the exact position of embedded fibre optic cables are difficult to control. By analysing curvature rather than the individual strain measurements, the influence of these uncertainties can be reduced. However, this requires that the distance between the fibre optic cables is known and remains approximately constant, meaning that a practical installation method for maintaining a defined sensor spacing would be needed.

In addition to the curvature distribution, local strain peaks measured by the DOFS were used to identify cracking in the top concrete layer. Such peaks also appear in the calculated curvature and can therefore provide information about both the location and distribution of cracks. Since DOFS can detect even small cracks in concrete, as shown in [24], the crack distribution was included as an additional indicator when distinguishing between the load types acting on the top concrete layer.

5.2 Shape sensor

This section presents the analysis used in Papers 4 and 5, as well as in the field test. The shape sensor analysis is based on strain measurements from DOFS installed along an aluminium rod or tube that acts as the sensor guide. The DOFS are positioned symmetrically around the cross-section of the sensor guide and bonded into milled or sawn slits. By evaluating the strain response from the distributed sensors, the analysis determines the direction of the load acting on the shape sensor, as well as its longitudinal, bending, and shear deformations.

For this type of sectional strain analysis, three sensors are theoretically sufficient to determine the strain state of the sensor guide, as they provide the minimum number of independent measurements required to resolve axial strain and bending in two directions. In the work presented in this thesis, however, both three and four DOFS were used in different experiments. When including an additional sensor, it provides redundancy in the measurement system, which is beneficial if one sensor is damaged, affected by local mea-

surement disturbances, or yields unreliable data.

Load direction

The DOFS mounted on the sensor guide provide strain measurements along the shape sensor, and the spacing between these measurements is governed by the gauge length of the sensing system. These measurements enable a sectional analysis of the shape sensor at each measurement along its length. When the shape sensor undergoes bending, the strain distribution across its cross-section varies systematically with the direction of deformation. The load direction can therefore be inferred by identifying the position around the sensor perimeter where the bending strain is largest. Following the method presented by Forbes et al [26], the strain measured by each DOFS is assumed to consist of a longitudinal strain component, ε_c, and a maximum bending strain component, ε_b. The longitudinal component is assumed to be uniform across the sensor cross-section, whereas the bending component reaches its maximum in the direction of the applied load. By dividing the bending component by the radius of the shape sensor, the curvature in the direction of the load is obtained. The strain components and load direction, θ, can therefore be obtained by solving the following system of equations:

$$\begin{aligned} \varepsilon_1 &= \varepsilon_c + \varepsilon_b \cos(\theta + \phi_1) \\ \varepsilon_2 &= \varepsilon_c + \varepsilon_b \cos(\theta + \phi_2) \\ \varepsilon_3 &= \varepsilon_c + \varepsilon_b \cos(\theta + \phi_3) \\ \varepsilon_4 &= \varepsilon_c + \varepsilon_b \cos(\theta + \phi_4) \end{aligned} \tag{5.2}$$

where ε_i is the strain measured by each DOFS and ϕ_i is the angle between the DOFS in the shape sensor. For the shape sensor used in the field test, the angles between the DOFS were $\phi_1 = 0°$, $\phi_2 = 90°$, $\phi_3 = 180°$, and $\phi_4 = 270°$. In Figure 5.1, the relation between the measured strain in ε_i and the strain components ε_c and ε_b is shown.

The system of equations in 5.2 is overdetermined as three unknowns and four equations are presented. The unknowns can, thus, in principle be resolved using three independent strain measurements. The additional measurement makes the estimation less sensitive to sensor noise, local strain disturbances, or loss of data from one fibre. It also enables the unknowns to be obtained using an overdetermined formulation, for example through a least-squares

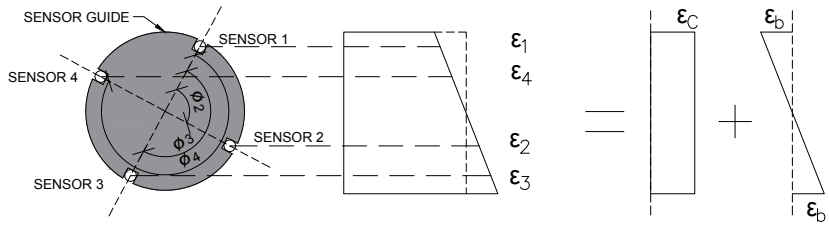


Figure 5.1: Sensor positions in a sensor guide and idealised strain distributions over a shape sensor section.

approach, which can improve the precision and reliability of the calculated sectional strain state.

The load direction along the shape sensor can be obtained by solving for θ which gives

$$\theta = \tan^{-1}\left(\frac{\varepsilon_4 - \varepsilon_2}{\varepsilon_1 - \varepsilon_3}\right) \tag{5.3}$$

Since the inverse tangent does not uniquely determine the quadrant of the load direction, the sign of the denominator must be considered when evaluating θ. If $\varepsilon_1 - \varepsilon_3 < 0$, the calculated angle should be adjusted by adding 180° to obtain the corresponding direction in the correct half-plane.

Bending deformation

The curvature of the shape sensor can be determined from the equation system in 5.2 by solving for ε_b, which represents the maximum bending strain at the circumference of the sensor guide, and dividing it by the radius of the sensor guide. This gives the curvature in the direction of the applied load, θ. However, this direction may vary due to measurement noise when the deformations are small. It may also vary at locations with localised deformation, such as at a rock joint, where the assumption that plane sections remain plane might be violated.

To obtain a consistent definition of curvature along the sensor, the curvature is instead evaluated separately in the vertical and horizontal directions. In each direction, a linear strain distribution is assumed according to $\varepsilon(y) =$

$\varepsilon_c + \chi y$, where y denotes the vertical or horizontal position in the cross-section, ε_c is the centroid strain, and χ is the curvature. The curvature is then obtained using a least-squares formulation, in which the expression in Eq. 5.4 is minimised.

$$\min_{\varepsilon_0,\chi} \sum_{i=1}^{4} (\varepsilon_i - (\varepsilon_0 + \chi y_i))^2 \tag{5.4}$$

The bending deflection of the shape sensor is then calculated by modelling the sensor guide as an Euler-Bernoulli beam. After applying the relevant boundary conditions, the slope $\phi(x)$ is obtained by integrating the curvature along the sensor length and the and bending deflection $v_b(x)$ is obtained by integrating the slope, where x denotes the longitudinal position along the sensor.

$$\phi(x) = \int \chi(x) dx \tag{5.5}$$

$$v_b(x) = \int \phi(x) dx \tag{5.6}$$

Shear and longitudinal deformation

In addition to curvature, the least-squares minimisation in Eq. 5.4 also provides the centroid strain of the sensor cross-section. If the shape sensor is not subjected to shear deformation, this centroid strain represents the longitudinal deformation along the sensor. However, when shear deformation occurs, and the shear strain is assumed to be constant over the cross-section, the measured centroid strain contains contributions from both longitudinal and shear deformation. In Figure 5.2, an infinitesimal element of a beam loaded by shear and normal loads are shown, where the centroid strain, ε_c, is decomposed to longitudinal strain, ε_l, and shear induced centroid strain, ε_s.

To decouple the strain components associated with longitudinal and shear deformation in the sensor guide, two assumptions are introduced, as further described in paper [F]:

1. Shear-induced centroid strain is localised within a shear zone
2. The centroid strain component from longitudinal deformation is distributed over a length longer than the shear zone

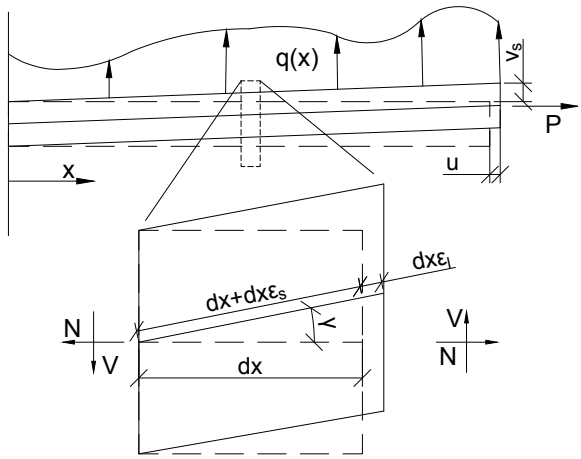


Figure 5.2: Infinitesimal element of a beam loaded by shear and normal forces, V and N respectively. Shear induced longitudinal strain, ε_s, and longitudinal strain, ε_l are induced in the element.

Based on these assumptions, strain from longitudinal deformation can be approximated over a shear zone by interpolation of strains from outside the shear zone. The remaining centroid strain within the shear zone is then interpreted as the contribution from shear deformation.

It should be noted that the shear zone must extend over a sufficient length to be detected by the DOFS. Consequently, an idealised direct shear deformation localised at a single plane cannot be captured directly using the presented method. Instead, the deformation must be distributed over a measurable shear zone along the sensor guide. This distribution is influenced by the design of the sensor guide and by its stiffness relative to the surrounding medium. By increasing the stiffness of the sensor guide, the deformation induced at a discontinuity may be spread over a longer length of the sensor, thereby increasing the shear-zone width and improving the possibility of detecting and quantifying shear deformation.

The shear zone can be identified by examining the curvature distribution along the shape sensor. When the sensor is subjected to localised shear de-

formation, e.g., across a rock joint, its behaviour can be compared to that of a dowel loaded in shear. Large forces are then induced on either side of the shear plane. Following the first assumption, the shear deformation is expected to occur in the region where these forces are concentrated. The location of the shear zone can therefore be inferred from the load, moment, and shear-force distributions along the sensor. The curvature is related to the bending moment according to

$$\chi = \frac{M}{EI} \tag{5.7}$$

where EI is the bending stiffness of the shape sensor. Since the shear force is obtained as the derivative of the bending moment, the corresponding shear force distribution can be evaluated from the curvature gradient as

$$\chi_s = \frac{d\chi}{dx} \tag{5.8}$$

The load distribution can be obtained by further differentiating the shear force distribution. However, the results in paper [E] and [F] showed that load distributions derived in this way are highly sensitive to sensor noise and variations in the shear force distribution. For this reason, the curvature and shear force distributions are considered more reliable indicators for identifying the shear zone. Figure 5.3 schematically illustrates the load, shear force, and moment distributions for a dowel, or rock-joint, load case. As shown in Figure 5.3d, the shear zone can be identified from the inflection points in the curvature diagram, together with the peak values in the curvature gradient distribution diagram shown in Figure 5.3c.

After the shear zones have been identified and the centroid strain components associated with shear and longitudinal deformation have been decoupled, the shear strain can be calculated as

$$\gamma = \cos^{-1}\left(\frac{1}{1+\varepsilon_s}\right) \tag{5.9}$$

where ε_s denotes the centroid strain component induced by shear deformation. The longitudinal and shear deformations, u and v_s respectively, are then obtained by integrating their corresponding strain components, γ and ε_l, along the length of the shape sensor:

$$v_s(x) = \int \gamma(x)dx \tag{5.10}$$

$$u(x) = \int \varepsilon_l(x) dx \tag{5.11}$$

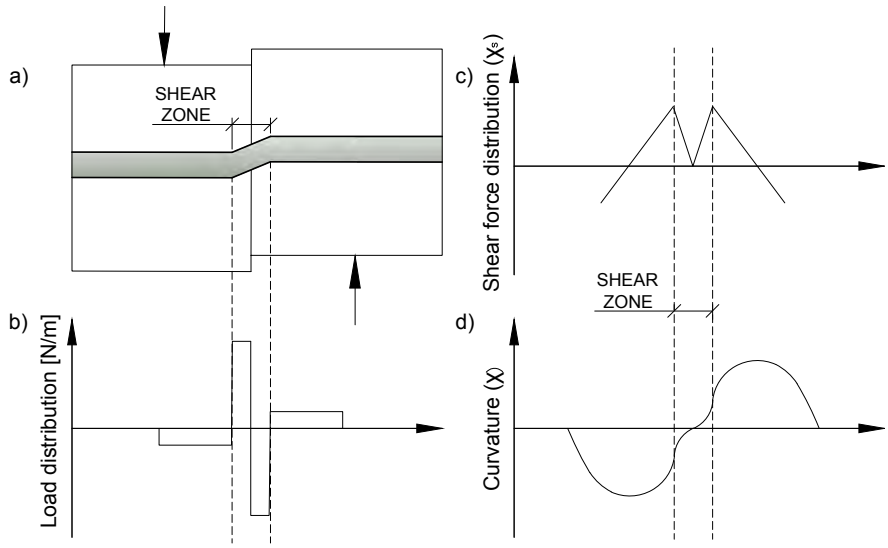


Figure 5.3: Schematically described behaviour of a shear loaded shape sensor. The a) load case, b) load distribution, c) shear force distribution, and d) curvature is shown.

CHAPTER 6

Results

This chapter presents summaries of the result from the experimental studies conducted in this thesis. The first part summarises the results from the laboratory experiments presented in the appended papers, while the second part presents previously unpublished results from the field test.

6.1 Lab experiments

Shotcrete experiments

The results from the experiments simulating loads on shotcrete linings include variations in load response and strain distributions measured using DOFS. The load response was evaluated in relation to all four factors included in the factorial design, while the strain distributions were compared with respect to the load type and surface treatment factors. Load and strain distributions obtained before peak load are presented in Paper [C], whereas the strain distributions after peak load are presented in Paper [D].

For the factors included in the factorial design, the top layer thickness was found to have the largest influence on the peak load. The load response was

also affected by the surface treatment, with higher loads generally obtained in specimens with hydro-demolished surfaces compared with specimens with ground surfaces. In addition, the cone-loaded specimens reached higher loads than the bag-loaded specimens. For the load size factor, increasing the loaded area resulted in higher loads for the cone-loaded specimens, whereas no clear influence on load magnitude was observed for the bag-loaded specimens.

Figure 6.1 presents the strain distributions and corresponding curvature for one bag-loaded specimen and one cone-loaded specimen. The two load conditions produce clearly different strain responses. In the bag-loaded specimen, tensile strains are measured in the top sensor over the loaded area and in the bottom sensor outside the loaded area, as seen in Figure 6.1a and c. Conversely, compressive strains are measured in the bottom sensor over the bag and in the top sensor outside the loaded area. This strain and curvature response resembles the behaviour of a beam subjected to a distributed load with restrained supports.

For the cone-loaded specimen, tensile strains are measured at both sensor levels as seen in Figure 6.1b and d, with larger magnitudes in the top sensor layer. The resulting curvature, Figure 6.1f varies across the loaded area, which is likely related to crack openings in the top concrete layer. The tensile strain measured in the sensors is most likely caused by the inclined load from the cone changing direction as it is transferred through the specimen.

After the peak load was reached, the specimens partially failed. The failure mode differed mainly depending on the load condition and on the surface treatment applied between the substrate slab and the top layer. In the cone-loaded specimens with ground surface treatment, complete loss of bond occurred between the substrate slab and the top layer. As a result, the residual load was carried only through the top layer and transferred to the steel bolts. In contrast, the cone-loaded specimens with hydro-demolished surface treatment exhibited only partial loss of bond between the concrete layers.

Figure 6.2 shows the curvature responses of the cone-loaded specimens prior and after peak load was reached. In specimens with a ground surface treatment, the curvature remains positive across the analysed region, indicating that the top layer primarily carries the residual load after bond loss. In contrast, for the hydro-demolished specimens, the curvature changes sign outside the loaded area. This sign change suggests that the bond between the substrate slab and the top layer remains partly intact, allowing the load to be

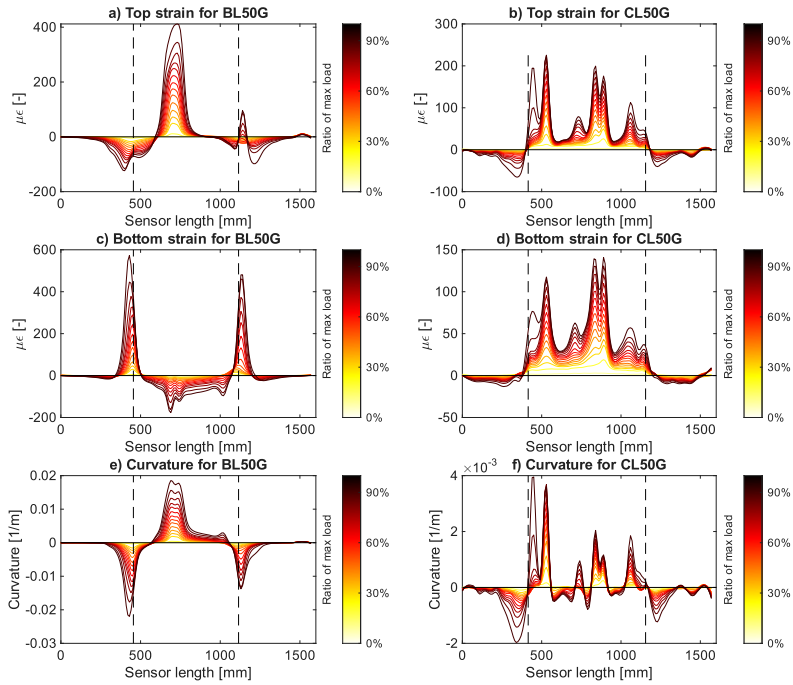


Figure 6.1: Strain distributions for a bag load specimen, a) and b), and a cone loaded specimen, b) and d). In e) and f), curvature distributions are shown for the bag and cone loaded specimen respectively.

transferred from the top layer to the substrate slab in a manner similar to the response observed in the bag-loaded specimens prior to reaching the peak load.

Figure 6.3 shows curvature distributions for the bag loaded specimens before and after the peak load. After the peak load was reached in the bag-loaded specimens with ground surface treatment, as well as in specimen BS50H, the bond nearest to the loaded area failed and was likely peeled from the substrate slab. This peeling response is observed in Figure 6.3a-c and e where the distance between the negative curvature peaks outside the loaded area increases as deformation develops. In the hydro-demolished specimens, however, both the negative and positive curvature peaks remain at approximately the same positions while their magnitudes increase. This indicates that the

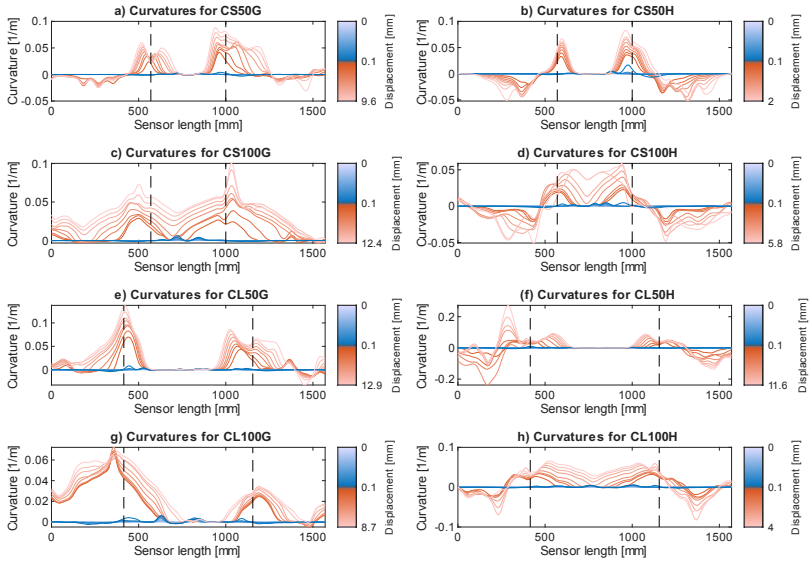


Figure 6.2: Curvature distributions for cone loaded specimens. Blue curves represent curvature prior to peak load and red curves after peak load was reached.

bond remains intact and that the top layer instead fails primarily in bending.

Shape sensor experiments

Papers [E] and [F] present the results from the two experimental studies involving shape sensors. The DOFS measurements were analysed using the method described in Section 5.2. This analysis provided the deformation of the shape sensor, which was then used to evaluate the deformation occurring along the shear planes in the experimental specimens.

In the first experiment, the cylinder-loaded concrete block that was instrumented with an aluminium tube sensor guide and 0.9 mm nylon-coated optical fibre cables, the specimen was loaded until a relative displacement of 4.3 mm developed between the cylinder and the surrounding concrete block. However, reliable DOFS data were only obtained up to a displacement of 3 mm and the test was stopped before any failure occurred in the specimen.

Figure 6.4 shows the bending, shear, and total deformation of the shape

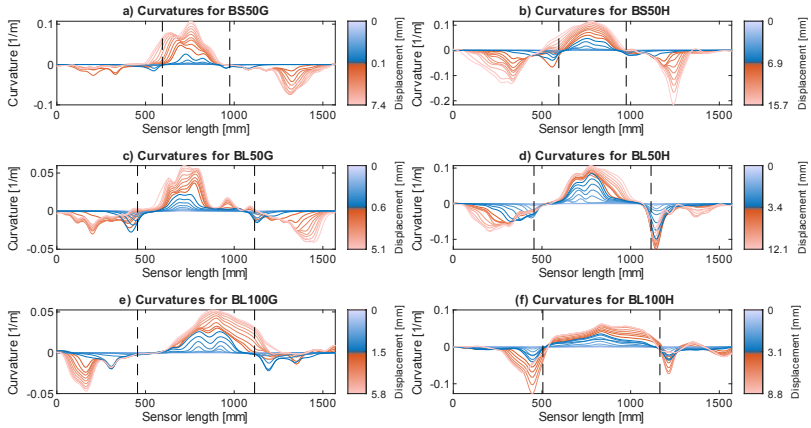


Figure 6.3: Curvature distributions for bag loaded specimens. Blue curves represent curvature prior to peak load and red curves after peak load was reached.

sensor along its length. Fixed boundary conditions were applied at the centre of the specimen, allowing the deformation on each side of this point to be attributed to the corresponding shear plane. Figure 6.4c also shows the deformation of the sensor guide obtained from 3D scanning after the test. This deformation cannot be compared directly with the deformation obtained through the DOFS since the test was continued until a cylinder displacement of 4.3 mm, whereas reliable DOFS data were only obtained up to 3 mm. Nevertheless, both the 3D-scanned deformation and the DOFS-based measurements show similar deformation modes, consisting of a combination of bending and shear deformation.

In the second experiment, the shape sensor consisted of an aluminium rod instrumented with both V9 sensor cables and acrylic-coated fibre cables. The sensor was tested in a setup comprising three separate concrete blocks, where shear deformation was induced by loading the middle block relative to the two outer blocks. The specimen ultimately failed by splitting of the middle block. Before failure occurred, the DIC system reached its data storage limit after recording a relative displacement of 2 mm between the middle and outer blocks, and the full deformation range could therefore not be captured.

In this specimen, the two cable types could be compared, and the results

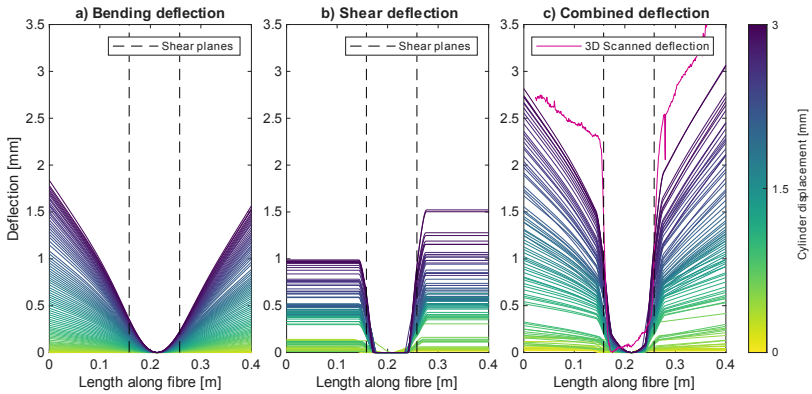


Figure 6.4: a) Bending, b) shear and c) combined deflection along the shape sensor in first shape sensor experiment.

show that both were able to provide reliable measurements at small deformations, between 0 and 0.2 mm. These strain measurements are presented in Figure 6.5, and it is clear that the measurements from the two cable types differ significantly. The strain measurements from the acrylic coated fibre cables localised around the shear planes, while the strain recorded in the V9 cables reach peak values approximately 50 mm before and after the shear planes.

Beyond approximately 0.2 mm, localised strain variations developed further in the acrylic-coated cables, and partial loss of data occurred along the shape sensor, particularly near the shear planes. This loss of data was not observed in the V9 cables. The localised variations and loss of data in acrylic coated sensor cables at the shear planes were likely caused by concentrated loads and deformation around the shear planes, which induced microbending in the fibre optic cable. The same phenomenon was not induced in the V9 fibre cables due to the more robust design including a thicker plastic sheath and protective metal tube.

Figure 6.6 compares the deformation of the sensor guide at one shear plane for both cable types with the deformation measured using DIC. The DOFS-based deformation was evaluated between the centre of the middle block and "Section 1", indicated in Figure 6.5. The start of the sensor was not used as the reference section because the outer blocks rotated during loading, and this rotation would introduce deformation not directly related to the shear plane

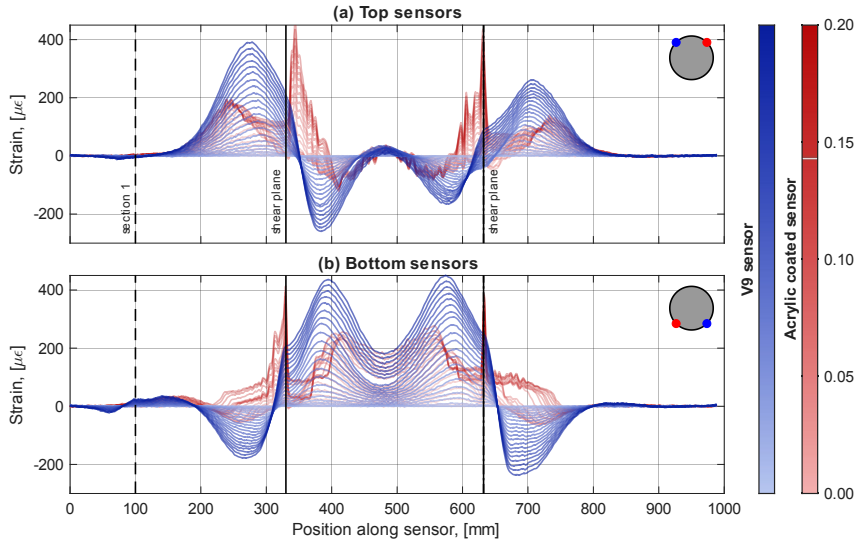


Figure 6.5: Strain measured in acrylic coated sensors and V9 sensors in the second sensor guide experiment.

response. "Section 1" was therefore selected as the reference location, since the strain response in the shape sensor begins to develop beyond this section, while remaining approximately zero before it.

For the acrylic-coated fibre cables, the shear deflection analysis presented in Section 5.2 could not be applied because localised strain variations developed around the shear planes. These variations prevented the shear zones from being identified from the curvature gradient. Instead, only the obtained bending deformation of the acrylic coated cables are shown in Figure 6.6. In contrast, the V9 fibre cables enabled the shear zones to be identified even at small deformation levels.

However, for middle-block deformations between 0 and 0.2 mm, the calculated shear deformation was larger than the deformation measured using DIC. This discrepancy is likely caused by a combination of factors. First, the conversion between shear strain, γ, and the shear-induced longitudinal strain, ε_s, in Equation 5.9 is highly sensitive to small variations in ε_s at low strain levels. Since the sensor noise remains approximately constant, at about $\pm 5\mu\varepsilon$, its relative influence becomes larger when the measured strains are small. Sec-

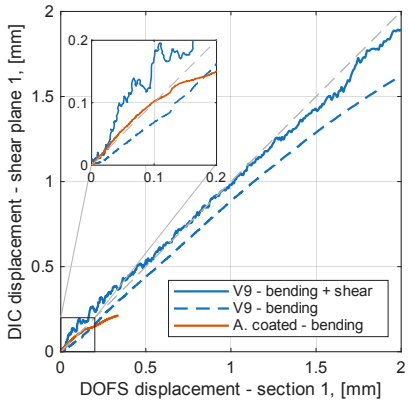


Figure 6.6: Shear plane deformation measured with DIC and DOFS.

ond, the algorithm used to identify the shear zone becomes less stable at small deformations, as further discussed in Paper [F]. If the identified shear zone is wider than the actual deformation zone, the calculated shear deformation will be overestimated.

To determine the direction of the load acting on the shape sensor in the second specimen, Equation 5.2 was applied to the measurements from the V9 sensors. Figure 6.7a shows the calculated load direction relative to the first sensor position, ϕ_1, defined in Figure 5.1. The load direction was evaluated for middle block deformations between 0 and 2 mm. At small deformations, where the measured strain magnitudes are low, the results show considerable variations. As the deformation increases, however, the load direction becomes more clearly defined. At the shear planes, the load direction changes by approximately π, which is expected because the support reactions act in the opposite direction to the applied load.

Changes in load direction were also observed near the ends of the shape sensor inside the outer concrete blocks. These changes were not expected, as their directions did not correspond to the support reaction or load direction. To reduce the influence of measurement noise and small, mechanically insignificant strain variations, the calculated load direction was filtered by excluding measurement points where the absolute strain magnitude was less than 4% of the maximum absolute strain magnitude in the shape sensor. The filtered results, shown in Figure 6.7b, indicate that the sensor guide was primarily

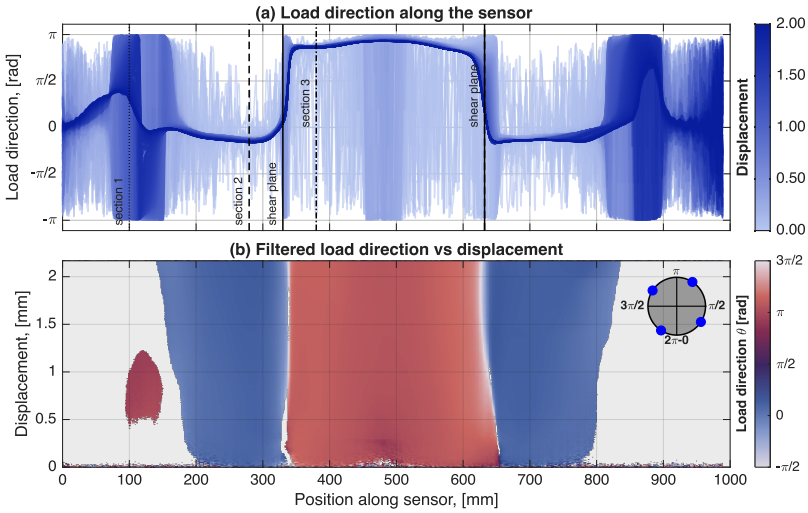


Figure 6.7: Load direction

loaded from two opposite directions.

6.2 Field test

The shape sensor was installed in the borehole on 28 February and grouted on 2 March. The first measurements were taken on 10 March, at which point the DOFS in the shape sensor were tared. The data presented in this thesis were recorded between 10 March and 21 May 2026, during which the tunnel excavation progressed as shown in Figure 4.1. At each measurement occasion, data were recorded from all DOFS in the shape sensor for approximately 10–20 minutes.

On 22 April, measurements were recorded continuously for 2 hours, during which a blasting event occurred. The results presented in the following sections are divided into two parts. First, the data and results from the blasting event are presented. This is followed by the data and results from the full measurement period.

Deformation during blasting

During the measurement on 22 April, data were recorded throughout a blasting event. The measurement lasted for 2 hours, with the blast occurring approximately 1 hour after the start of the recording. To reduce the influence of measurement noise, the strain response was evaluated using temporal mean strain values calculated separately for the periods before and after the blast. These mean strain values are shown in Figure 6.8, where the measurements are tared to the first measurement during the blast event and a moving mean with a 13 mm window size has been applied to the data. The measured strain magnitudes were relatively small, with peak values of approximately $10\mu\varepsilon$. Nevertheless, four segments along the shape sensor could be identified where strain changes occurred during the blast, located at approximately x = 0.4 m, x = 1 m, x = 3 m, and x = 5 m. At the first three positions, the strain is localised in tensile peaks while at x = 5 m, more distributed compressive strain variations occur.

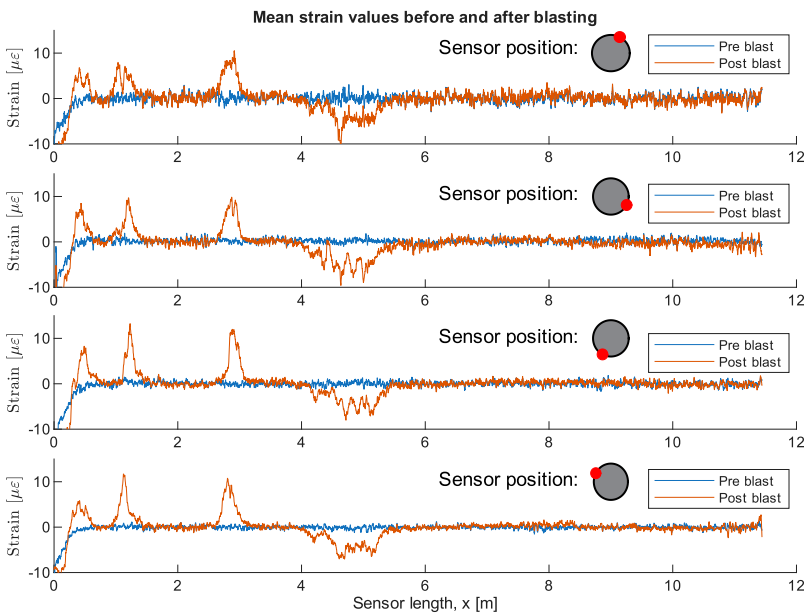


Figure 6.8: Mean strain values measured before and after blasting for each sensor.

The measured strains in Figure 6.8 show that tensile and compressive strains occur at the same positions in all four DOFS along the shape sensor. Where tensile strains are observed, the response is likely associated with longitudinal or shear deformation rather than bending, since bending would generally produce strains with opposite signs or different magnitudes across the sensor cross-section. In the compressed zone, however, the strain magnitudes differ slightly between the sensors, indicating that bending deformation is also induced while the shape sensor is simultaneously subjected to compression. This response may be explained by the deformation of the rock mass induced by the blasting, which is acting towards the excavated tunnel as the stress-strain state is redistributed. The deformation appears within the compressed zone of the sensor, possibly because the rock mass in this region might have been fractured and therefore more susceptible to local deformation.

Figure 6.9 shows the centroid strain, vertical curvature, and gradient of the vertical curvature for the strains measured after blasting over the first 6 m of the sensor, which includes all four identified strain changes. The same results could also be presented for the horizontal direction; however, they are omitted here because they show similar strain patterns. Consistent with the raw strain data in Figure 6.8, the centroid strain increased around x = 0.4 m, x = 1 m, and x = 3 m, while it decreased around x = 5 m. Curvature changes were also observed in all four sections. Around x = 1 m and x = 3 m, the curvature response resembles dowel action. However, examination of the curvature gradient, as described in Figure 5.3, confirms dowel action only around x = 1 m, whereas the response in the other sections is less distinct.

In the sections around x = 0.4 m and x = 5 m, no clear changes in curvature or distinct peaks in the curvature gradient are observed which could indicate dowel action, suggesting that the response is governed by longitudinal deformation and some bending. Around x = 3 m, the curvature response suggests possible dowel action of the shape sensor. However, the curvature gradient shows only one distinct peak, which may indicate that the shear deformation is too localised for a shear zone to be clearly defined. This behaviour is likely related to the high stiffness ratio between the shape sensor and the surrounding rock. When this ratio is high, the load and deformation are distributed over a shorter length of the shape sensor adjacent to the shear plane. In addition, for shear deformation to be distributed over a wider shear zone, crushing of the rock within the shear zone is required. In high-quality rock subjected to

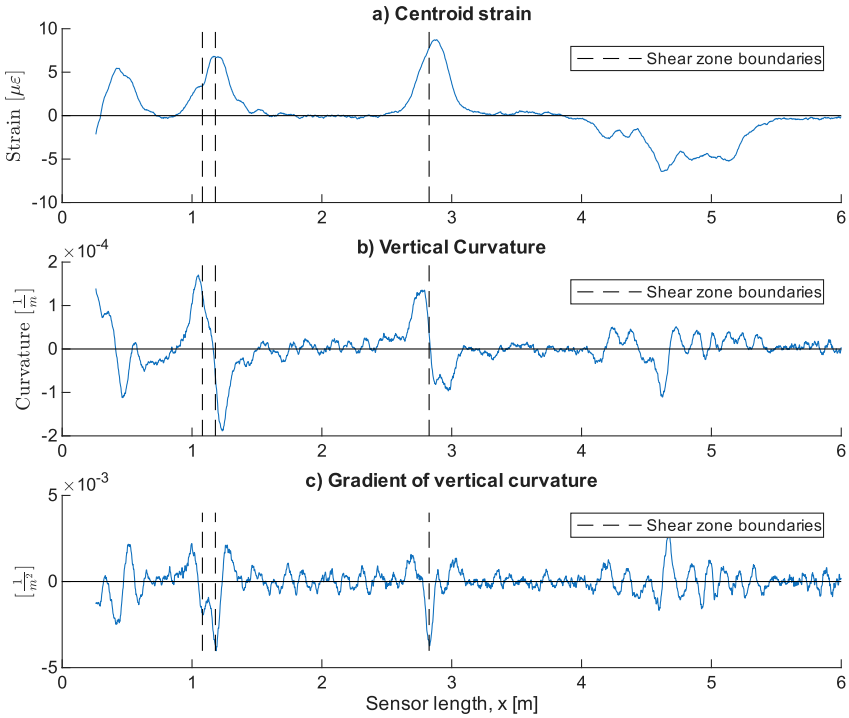


Figure 6.9: a) Centroid strain, b) vertical curvature and c) gradient of vertical curvature for the shape sensor. Boundaries of shear zones identified along the shape sensor are also included.

a triaxial stress state, the aluminium sensor guide may not generate sufficient load to induce such crushing.

The difference between the responses at x = 1 m and x = 3 m may be related to their positions relative to the tunnel wall. At x = 1 m, the shear deformation occurs closer to the free tunnel wall, which may allow longitudinal deformation, or dilation, along the rock joint to propagate towards the free tunnel wall. In contrast, the rock joint at x = 3 m is more confined by the surrounding rock mass, which may limit the amount of dilation that can develop. Differences in crack geometry may also contribute to the observed response; for example, the joint at x = 1 m may be wider or more open than the joint at x = 3 m.

As noted above, the strain magnitudes measured by the sensors, and consequently the derived centroid strains, are very small. When these centroid strains are decoupled into longitudinal and shear components according to the procedure described in Chapter 5, the resulting shear-induced centroid strains are also small. Under these conditions, the shear strain calculated using Equation 5.9 becomes highly sensitive to small variations in the input strain, because the inverse cosine term varies rapidly as its argument approaches 1. Consequently, minor measurement variations or noise in ε_s can lead to considerable variation in the calculated shear strain. The shear deformation obtained for small shear-induced strains should therefore be interpreted with caution, as also discussed in Papers [E] and [F].

Because the calculated shear deformation is small and sensitive to measurement uncertainty, it is omitted from further analysis of deformation. Figure 6.11 presents the vertical and horizontal bending deformation together with the longitudinal deformation along the shape sensor and the direction of the calculated deformation is presented in Figure 6.10. The vertical and horizontal deflections remain relatively constant until approximately x = 4.5 m, where the sensor deflects downward and towards the excavated tunnel. The shape sensor is elongated at the identified shear planes, as indicated in Figure 6.9, and compressed over the section where bending deformation occurs.

For the deformation calculation, cantilever boundary conditions were applied at x = 0.26 m. This position was selected to reduce the influence of temperature changes caused by increased ventilation in the service tunnel before and after blasting. The applied boundary conditions assume both zero displacement and zero slope at x = 0.26 m. Consequently, the method pro-

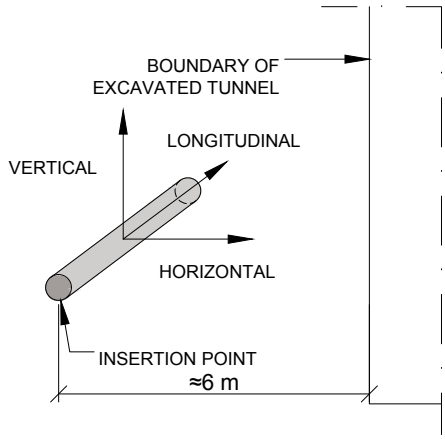


Figure 6.10: Position of the shape sensor with regards to the excavated tunnel shown schematically with definitions for directions of calculated deformation in the shape shape sensor.

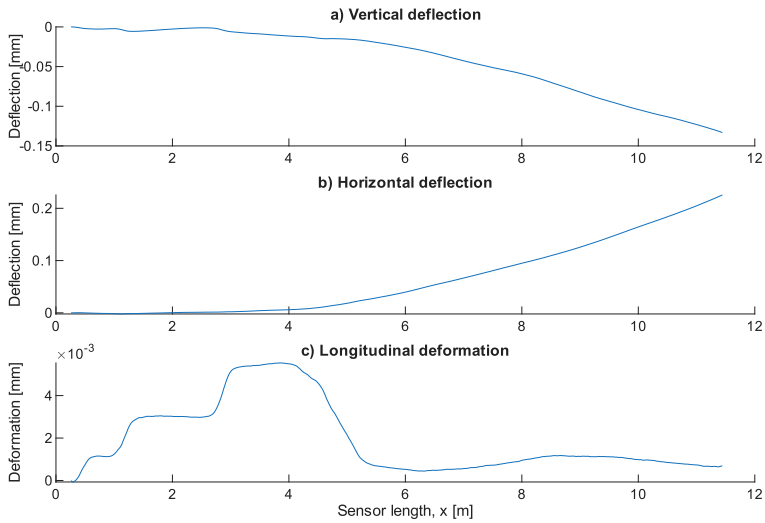


Figure 6.11: Calculated deformation in the shape sensor including a) vertical and b) horizontal bending deflections and c) longitudinal deformation.

vides only the relative displacement along the shape sensor, while rigid-body deformation is not captured. Such deformation could, however, be included if both the displacement and slope of the shape sensor were measured at the rock-wall insertion point with, e.g., an accelerometer and tiltmeter.

It should also be noted that, by applying cantilever boundary conditions, the calculated deformation is cumulative. As a result, the accuracy of the calculated deformation decreases with distance along the shape sensor. The error is mainly caused by noise in the DOFS measurements, which varies by approximately $\pm 5\mu\varepsilon$. To reduce the influence of this noise, mean values from several measurements were used in the calculation. The accumulated error could be further reduced by applying boundary conditions at a position farther along the shape sensor, closer to the section of interest.

Before and after x = 4.5 m, the vertical and horizontal bending deformations are approximately linear. This may indicate that two separate rock blocks, or rock masses, are deforming relative to one another around this section. Since the compression in the shape sensor is distributed over a length of approximately 1 m, the deformation does not appear to be localised at a distinct rock joint. Instead, the response suggests deformation over a weak zone between adjacent rock blocks or rock masses.

Full monitoring scheme

Monitoring with the shape sensor began on 10 March, and the final measurement was taken on 21 May 2026. Data were recorded at approximately one-week intervals during this period, and the extent of excavation at each measurement occasion is shown in Figure 4.1. During each measurement occasion, the strains recorded by the DOFS remained nearly constant, apart from measurement noise. To reduce the influence of noise and enable comparison between measurement occasions, the mean strain was calculated for each measurement period. For the measurement that included a blasting event, the data recorded before and after the blast were treated separately when calculating the mean strains.

The mean strain for each measurement occasion is shown in Figure 6.12. Examination of the strains along the full sensor length shows that the strain magnitudes increase as the excavation progresses, while the positions of the strain changes remain largely unchanged. This indicates that the DOFS measure increasing strain magnitudes during excavation, and that the deformation

mode remains approximately constant. Compared with the strains recorded during the blasting event shown in Figure 6.8, the strain localisations over the full measurement period are more numerous and more distributed along the shape sensor. Between x = 0 m and x = 0.5 m, all DOFS show a nearly uniform strain increase. This response is most likely related to a change in temperature. For aluminium, a strain increase of $150\mu\varepsilon$ corresponds to a temperature change of approximately 6.5°C, which is a reasonable mean temperature increase between March and May in Gothenburg.

Figure 6.13 presents the centroid strains, together with the vertical and horizontal curvatures, all calculated using Eq. 5.4 for the first 6 metres of the shape sensor. The initial strain increase between x = 0 m and x = 0.5 m is, as stated above, most likely caused by a temperature increase, as the centroid strains increase in this section while the curvatures remain largely unchanged. Around x = 5 m, increased compressive strains are observed relative to the rest of the sensor. This compression is consistent with the compressive response recorded during the blasting event, as shown in Figure 6.9a.

Comparison of Figures 6.13b and c shows that curvature is induced in both directions of the shape sensor. Although the curvature varies considerably along the sensor length, no distinct shear plane can be identified. This may be because the rock mass closest to the tunnel wall was fractured during excavation, resulting in closely spaced rock joints. The short spacing between joints may cause the bending direction to alternate along the sensor, making it difficult to distinguish individual shear planes.

Figure 6.14 presents the bending deflection and longitudinal deformation for all measurement occasions. Since no shear zones could be identified, shear deformation was not included in the calculated deformation. As in the deformation calculation for the single blasting event, cantilever boundary conditions were applied at x = 0.26 m to reduce the influence of temperature changes near the rock wall. The overall deformation mode is similar to that observed during the single blast, as shown in Figure 6.11. In the longitudinal deformation, tensile deformation occurs near the beginning of the sensor, while compressive deformation is observed around x = 5 m. The horizontal deflection remains small until approximately x = 5 m, after which it increases. The vertical deflection, however, does not correspond as closely to the response observed during the single blasting event. Over the full monitoring period, the results indicate that part of the vertical deflection is positive.

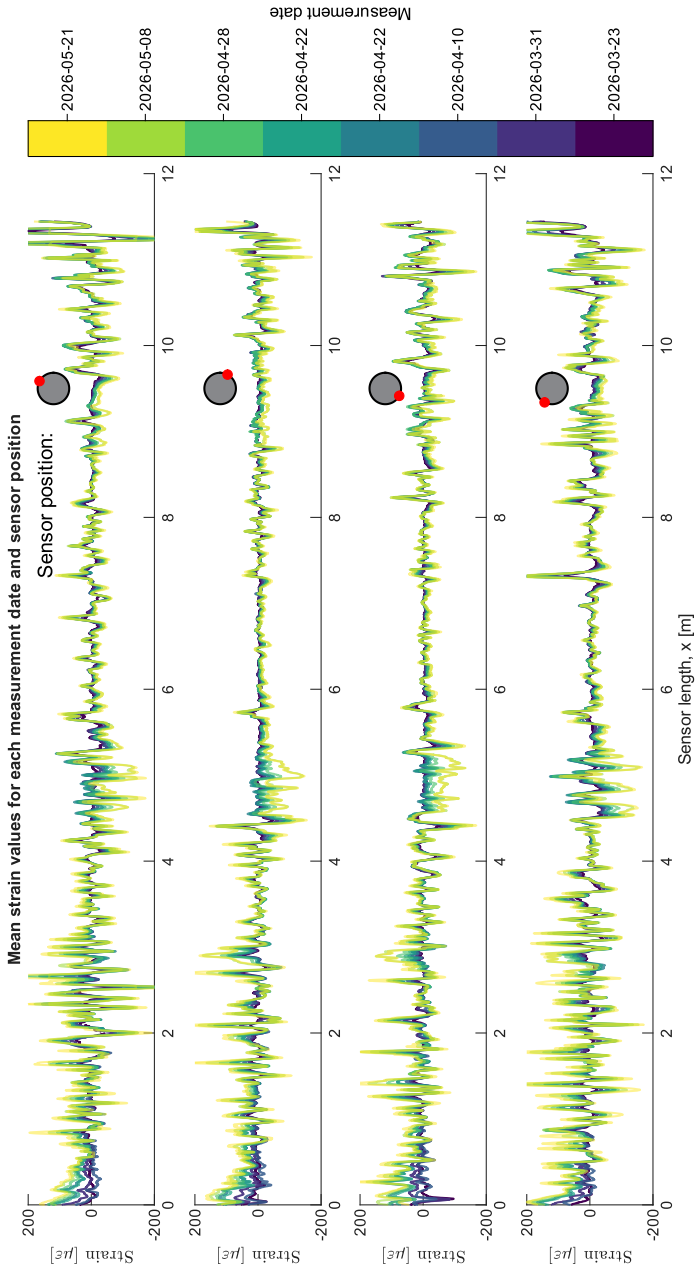


Figure 6.12: Mean strain values along each sensor for every measurement occasion. The sensor position shown in each graph as a red dot on a schematically drawn shape sensor.

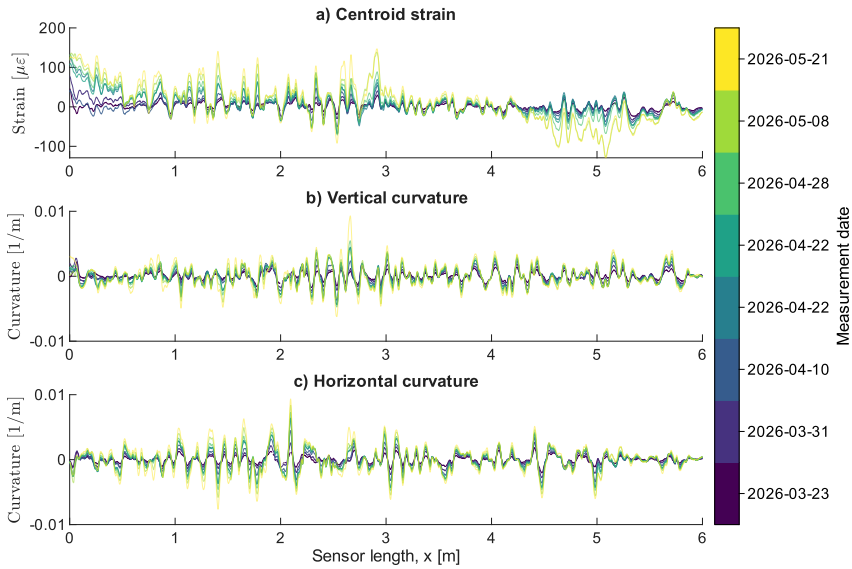


Figure 6.13: Mean values at each measurement date for a) centroid strain, b) vertical curvature and c) horizontal curvature for the 6 first meters of the shape sensor used in the field test.

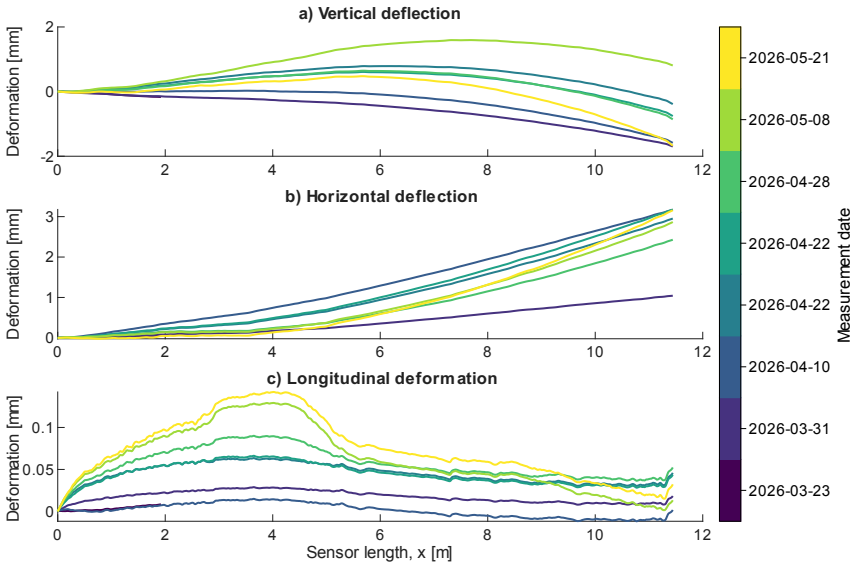


Figure 6.14: a) Vertical deflection, b) horizontal deflection and c) longitudinal deformation along the shape sensor.

It is unlikely that the rock mass deformed upward during excavation. However, as the tunnel was excavated and stresses were redistributed, a local stress reduction around the shape sensor may have produced a small upward deformation. A more likely explanation is that larger downward deformation occurred near the beginning of the sensor, at x = 0.26 m. Since the cantilever boundary conditions only provide relative deformation along the sensor, this downward deformation may cause the calculated response farther along the sensor to appear as upward deformation, even though this does not necessarily represent the absolute deformation of the rock mass.

Furthermore, the deformation accumulated over the full monitoring period is more distributed along the shape sensor than the deformation recorded during the single blasting event. This is particularly evident when comparing the longitudinal deformation in Figure 6.14c with that in Figure 6.11c, where the long-term deformation is more spread out rather than localised at potential rock joints.

The distributed deformation observed over the full monitoring period may

result from time-dependent deformation of the rock mass after blasting. Excavation disturbs the initial equilibrium of the rock mass, and deformation is induced as a new equilibrium state develops. This process is likely gradual rather than instantaneous, causing initially localised deformations to redistribute over time. In addition, several blasts were carried out between the measurement occasions. Each blast may have activated deformation along different joints, which could further contribute to the distributed deformation observed between measurements.

CHAPTER 7

Discussion

7.1 Rock substitutes and laboratory limitations

The laboratory experiments conducted in this thesis were intended to reproduce load and deformation mechanisms relevant to hard rock conditions. However, reproducing in situ hard rock behaviour in a laboratory setting is challenging. Natural rock masses are inherently non-uniform, and their mechanical response is influenced by factors such as joint geometry, geological history, mineral composition, and stress state. This variability would make it difficult to achieve reproducible experimental conditions and to compare results between specimens, as local heterogeneities could introduce large variations in the measured response. In addition, reproducing representative in situ stress-strain conditions at the scale of the experiments would require substantially larger specimens and a more advanced laboratory setup than was available for this work.

Rather than attempting to reproduce full in situ hard rock conditions, the experiments were designed to represent the relevant load and deformation mechanisms under controlled laboratory conditions. For this purpose, rock was substituted with concrete. This substitution reduced the variability asso-

ciated with natural rock heterogeneity and made it possible to conduct more reproducible experiments with better control over specimen geometry, material properties, boundary conditions, and loading procedures.

Since the experimental specimens were designed to simulate selected mechanisms that may occur in rock during tunnel construction, the results should be interpreted in relation to these controlled conditions. The experiments can therefore demonstrate whether DOFS are capable of capturing the simulated load and deformation mechanisms, but they cannot by themselves verify that the same mechanisms occur in an in situ rock mass. The relevance of the results depends on the extent to which comparable load and deformation mechanisms develop under field conditions.

Field tests are therefore needed to verify whether the load and deformation mechanisms simulated in the experiments are representative of field conditions. For the shotcrete lining monitoring application, no such field verification was included in this work. Verifying these mechanisms in a field setting would require DOFS to be installed in a tunnel section where the shotcrete lining is subjected to significant loading. Such conditions can be difficult to identify during tunnelling, since potentially unstable blocks are commonly stabilised by additional rock bolts before large loads develop in the lining. For the shape sensor, the field test presented in Chapter 4 was conducted to verify that the experimental behaviour also occurs under field conditions.

7.2 Shotcrete linings

The results from the simulated shotcrete lining experiments show that the two load cases can be distinguished under controlled laboratory conditions. Both strain distributions and curvature distributions differ significantly between the two load cases. In a real tunnel lining, however, the strain measured by DOFS would also include contributions from other sources, such as shrinkage, temperature changes, and ground deformation. These additional strain components would make it more challenging to isolate the strain response associated with a specific load case. This is particularly relevant for a loose rock block, represented in the experiments by the cone-loaded specimens, where the strain magnitudes before failure were relatively small. In addition, the resulting strain distribution may resemble crack-induced strain patterns caused by other mechanisms, making load-related strains more difficult to identify in

field measurements.

Compared with conventional techniques for inspecting and monitoring shotcrete linings, DOFS can provide more detailed and direct information about the structural behaviour and condition of the lining. Unlike point-based monitoring systems, distributed measurements reduce the need to know the exact locations of load concentrations before installation. However, as shown in Paper [C], the sensor must still pass through the loaded region to capture the associated strain and curvature response. Monitoring entire tunnels using Rayleigh-based OFDR would therefore require dense sensor coverage, which may lead to impractical and costly installations. A more suitable application may be targeted monitoring of weak zones or tunnel sections with complex geometries, such as intersections, where improved information about loads and deformation could contribute to improved safety and control during tunnelling. For longer monitoring distances, other DOFS techniques, such as Brillouin-based systems, may provide an alternative, although generally with lower spatial resolution.

7.3 Shape sensor prototyping

The first shape sensor design and test were presented in [47]. This initial prototype consisted of an aluminium tube instrumented with nylon-coated sensor cables bonded using silicone adhesive. The results showed that the silicone adhesive did not provide sufficient bond strength to transfer strain reliably from the sensor guide to the DOFS. The adhesive was therefore replaced with a two-component epoxy, and the first experimental specimen described in Section 3.2 was subsequently designed.

Because the DOFS stopped providing reliable data after 3 mm of displacement, further design improvements were required to increase the measurable deformation range. It should also be noted that the stiffness ratio between the sensor guide and the concrete loading elements in the first experiment was small compared with what would be expected for a real rock discontinuity. Since this stiffness ratio is likely to be higher in field applications, data loss was expected to occur at even smaller deformations under in situ conditions.

To test other combinations of sensor guides and sensor cables, two steel test fixtures were built. Each fixture consisted of two 20 mm thick steel plates welded perpendicular to a steel base plate. The spacing between the

two welded plates was 75 mm in one fixture and 55 mm in the other. This arrangement allowed the fixture with the smaller plate spacing to fit inside the fixture with the larger plate spacing, as seen in Figure 7.1. Holes were drilled through the welded steel plates to accommodate the shape sensor. By installing a shape sensor through the holes and pulling the two fixtures apart, shear deformation was induced in the sensor between the welded plates.

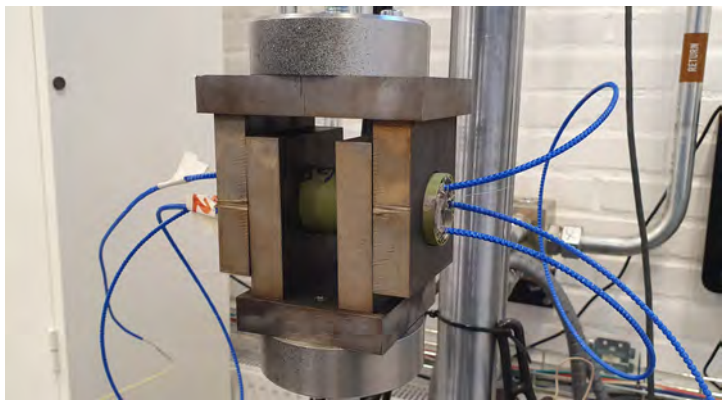


Figure 7.1: Test setup for shape sensor prototyping. In this figure, a 3D-printed sensor guide is tested with BRUsens V9 cables.

In these preliminary tests, several sensor guide prototypes were evaluated. Both the sensor guide geometry and the type of optical fibre cable were varied. The tested sensor guides included PVC and PA plastic pipes, 3D-printed plastic tubes with predefined slits for the fibre optic cables, and aluminium tubes and rods with milled slits. Some of the tubular sensor guides were tested both with and without concrete cast inside the tube. The tested fibre optic cables included 0.25 mm acrylic-coated fibres, 0.9 mm nylon-coated fibre optic cables, and robust 3.2 mm BRUSens V9 cables.

The preliminary tests showed that the 3D-printed plastic tubes were too brittle for the intended application. As the tubes failed, the sensors detached from the sensor guide, preventing reliable strain transfer. The PA and PVC tubes exhibited more favourable plastic deformation behaviour in shear. However, when the milled slits were too large, deformation became localised in the weakened tube walls. Consequently, the thicker BRUSens V9 cable could not be combined effectively with the plastic tubes. When acrylic and nylon coated

fibre optic cables were used with the plastic tubes, loss of data occurred at small deformations, most likely due to microbending in the cables, similar to the behaviour reported in Paper [F] and seen in Figure 6.5.

For the aluminium tubes, data loss occurred after larger deflections compared to the 3D printed and plastic sensor guides for both the acrylic and nylon coated cables. For the aluminium rod, only small deformations developed before the maximum load capacity of the test machine was reached. Since reliable data could be obtained over a larger deformation range when using a stiffer sensor guide and more robust fibre optic cables, the aluminium rod combined with BRUSens V9 cables was selected for the main experimental specimen. Acrylic coated fibres were also included with the aluminium rod, as this combination had not been evaluated in the preliminary tests and the increased stiffness of the sensor guide was expected to improve the measurable deformation range.

7.4 Shape sensor field applicability

The results of the field test demonstrate that the relative deformation along the sensor guide can be measured when the shape sensor is installed in a rock mass. However, determining the total deformation of the shape sensor requires more clearly defined boundary conditions. This could be achieved by measuring both the translation and rotation of the sensor at the insertion point. Alternatively, the shape sensor could be installed from a location farther away from the tunnel, where deformation may be assumed to be close to zero, allowing the boundary conditions to be applied at that position.

In the presented field application, shear deformation in individual rock joints could not be quantified. This was partly due to the small measured strain magnitudes, which limited the accuracy of the calculated shear deformation, and partly due to the potentially short spacing between discontinuity planes in the rock mass. Nevertheless, the results from the single blasting event indicated localised deformation that may be associated with shear deformation and discontinuity planes. Because continuous measurements were utilised during this event, the strain response before and after blasting could be evaluated in greater detail. Applying continuous monitoring throughout the full excavation process, including all blasting events, could therefore make it possible to capture the strain distribution associated with each blast and to study the

potential redistribution of deformation over time, potentially enabling quantification of shear deformation.

The results from the single blasting event also indicate that the rock mass surrounding the shape sensor may be too stiff at around 3 m from the beginning of the sensor, or may have too high a strength for the crushing of the rock to occur in the vicinity of a potential discontinuity plane. The sensor guide used in this application was a 40 mm diameter aluminium rod, which is relatively soft and weak compared with, for example, a steel rod. Replacing the aluminium rod with a high-strength steel rod could increase the stiffness and strength of the sensor guide. This may help distribute deformation from a direct shear plane over a wider shear zone, thereby improving the possibility of quantifying shear deformation. However, this would also increase the weight of the sensor by a factor of 5 which would make installation of the shape sensor more difficult.

The load direction calculation was also applied to the field test data. However, the results are not presented here because the calculated load directions varied considerably along the sensor and between measurement occasions, making them difficult to interpret in a mechanically meaningful way. This variability is likely related to the small deformation and strain magnitudes measured in the field test. At such low strain levels, the load direction calculation becomes sensitive to measurement noise and small local variations in the strain response. The variation in load direction may also be caused by loads acting on the shape sensor from multiple directions, making it difficult to identify a single dominant loading direction. Further analysis is therefore required before the load direction results from the field test can be used to draw reliable conclusions about the loading or deformation direction in the surrounding rock mass.

CHAPTER 8

Conclusions and Future Work

8.1 Conclusions

In this thesis, DOFS were applied in two underground infrastructure monitoring applications. In the first application, DOFS were embedded in experimental shotcrete lining specimens to identify load types acting on shotcrete tunnel linings in hard rock. In the second application, a DOFS-based shape sensor was developed, together with a method for determining shear deformation in the sensor, with the aim of measuring deformation in the rock mass surrounding an underground excavation. The conclusions from the thesis are structured according to the objectives presented in Chapter 1.

Objective 1 - *To identify load types acting on shotcrete tunnel linings in rock tunnels using DOFS.*

Two load types acting on shotcrete linings were investigated: a rock block load and a distributed load combined with bond loss between the shotcrete and the tunnel surface. The load types were studied experimentally using specimens in which the rock was represented by a concrete substrate slab and the shotcrete

was replaced by cast fibre-reinforced concrete. The results showed that the two load types could be distinguished using DOFS. This was achieved through a one-directional curvature analysis based on two aligned DOFS installed in the shotcrete layer at different distances from the substrate slab.

The load types could be identified before the maximum load was reached in the specimens. This indicates that a monitoring system based on DOFS has the potential to provide early warning before failure and support pre-emptive maintenance. However, identifying the load type requires that the pair of DOFS crosses the loaded area of the lining. For a reliable monitoring system, the DOFS would therefore need to be installed with sufficiently small spacing to capture local behaviour and load effects throughout the monitored tunnel section.

Objective 2 - *To demonstrate the adequacy of advanced sensor-based monitoring systems for obtaining unique and trustworthy data in shotcrete tunnel linings.*

The experimental studies showed that distributed optical fibre sensing can provide information that is difficult, or not possible, to obtain using conventional point-based monitoring methods. By embedding DOFS in the specimens, distributed strain profiles could be measured with high spatial resolution during loading. This made it possible to identify both local strain concentrations and broader structural response patterns, demonstrating that the monitoring system can capture spatially continuous information relevant to local failure mechanisms in shotcrete linings. The one-directional curvature analysis also made it possible to distinguish between intact bond, progressive delamination, and more abrupt loss of composite action between the lining and the substrate. In this way, the sensor data were not only descriptive but could also be linked to identifiable structural mechanisms.

Objective 3 - *To devise a DOFS-based sensing system suitable for measuring deformations in rock induced by tunnel excavation.*

This objective was addressed through the development, laboratory evaluation, and field implementation of a DOFS-based shape sensor intended for deformation monitoring in rock masses. The final shape sensing system consisted of

a 40 mm diameter aluminium rod with four BRUsens V9 optical fibre cables mounted longitudinally along the rod. By measuring strains in the optical cables during deformation, the sectional strain distribution along the sensor could be derived. This distribution was then used to calculate curvature, centroid strain, and load direction along the sensor, which together enabled the deformation of the shape sensor to be evaluated.

The laboratory studies showed that the shape sensor concept is suitable for capturing localised deformation mechanisms representative of rock discontinuity deformation. They also showed that both the design of the sensor guide and the choice of optical fibre cable strongly influence the quality and reliability of the measurements. Robust multilayer cables provided smoother and more stable strain profiles and remained functional over larger deformation ranges, making them more suitable for practical field applications.

The field test demonstrated that the developed shape sensor can be installed in a borehole adjacent to an active tunnel excavation and withstand the practical constraints of a drill-and-blast environment. The results showed that the sensor can provide relative bending and longitudinal deformation in the surrounding rock mass. The field test also clarified practical limitations of the system. For example, the high stiffness and strength of the rock mass surrounding the sensor appeared to limit the development of a clearly identifiable shear zone in some sections.

Objective 4 - *To develop a method for detecting, locating, and quantifying shear deformations utilising longitudinal strains measured in the sensing system.*

The developed method for addressing this objective is based on beam theory and utilises the displacement field from Timoshenko-Ehrenfest formulations and uses the strain measurements in the shape sensor to calculate curvature, identify shear zones, decouple longitudinal and shear-induced strain components, and quantify deformation contributions from bending, longitudinal deformation, and shear. Laboratory studies demonstrated that shear planes can be detected and located from characteristic strain and curvature responses in the shape sensor. In particular, the gradient of the curvature proved to be a reliable indicator for identifying the position and width of shear zones, as local maxima and minima developed around the imposed discontinuity planes.

The developed method also enabled shear deformation to be quantified by separating the centroid strain into longitudinal and shear-induced components. By assuming that shear-induced strain is localised within a shear zone, while longitudinal deformation is distributed over a longer length, the longitudinal strain contribution could be interpolated across the shear zone and subtracted from the measured centroid strain. The remaining strain component was then used to calculate shear strain and consequently shear deformation.

In the field test, the method could identify indications of localised deformation and possible shear-related behaviour during a blasting event. However, shear deformation in individual rock joints could not be quantified reliably in the field application. This was mainly due to small strain magnitudes, measurement sensitivity at low strain levels, possible short spacing between discontinuities, and the high stiffness and strength of the rock mass surrounding the sensor. The methods practical application requires sufficient deformation magnitude, appropriate sensor stiffness, and continuous measurements during excavation events.

8.2 Future work

For the first application studied in this thesis, monitoring loads acting on shotcrete linings, the experimental work was carried out using substitutions for both rock and shotcrete. The rock was represented by a concrete substrate, while the shotcrete was replaced by cast fibre-reinforced concrete. In addition, the cast lining layer was not confined as it would be in a real tunnel, and the experiments were conducted at a reduced scale compared to a real tunnel. These factors may influence the strain behaviour in the lining compared with field conditions. Therefore, the experimental findings should be verified through field testing. A future field test with DOFS embedded in a shotcrete lining could also improve understanding of the structural behaviour of shotcrete linings in hard rock and provide data that support empirical design methods.

However, controlling the load and deformation in the field, and ensuring load conditions comparable to those in the laboratory experiments, would require extensive planning and access to the underground excavation. Such access is difficult to obtain in an ongoing commercial tunnel project, where schedules are typically tight and budgets are limited. In addition, accessing

parts of the tunnel before shotcrete has been applied involves significant safety risks due to the possibility of rock fall from the tunnel crown.

Because such field tests are difficult to perform, a suitable first step would be to calibrate a numerical model using the experimental results presented in this thesis. The calibrated model could then be applied to more realistic conditions, including the effects of scale, confinement of the shotcrete layer, and representative boundary conditions.

For the second application, shape sensing in hard rock conditions, further analysis of the field test should be conducted by comparing the sensor results with conventional monitoring data collected by the contractor during tunnel excavation. Such data may include tunnel convergence measurements and extensometer readings from the rock mass above the tunnel. A further analysis of more appropriate boundary conditions should also be carried out, where conventional monitoring data could be used to validate the deformation calculations.

Further work should also address shape sensor design. In particular, the stiffness and strength relationship between the monitored medium and the sensor guide should be investigated to improve sensor design and ensure that a sufficiently long shear zone can develop when shear deformation occurs along a discontinuity. This could be studied through additional experimental campaigns or through numerical parametric analyses.

The method presented in this thesis only considers shear deformation occurring perpendicular to the shape sensor. Further development is therefore required to account for shear deformation in discontinuities that intersect the sensor at other angles. In addition, methods are needed for interpreting shear deformation when cracks or discontinuities are closely spaced along the length of the shape sensor, as this may affect the ability to distinguish individual deformation zones and accurately quantify the deformation occurring in the sensor.

References

[1] A. M. M. Wood, *Tunnelling : management by design*. E & FN Spon, 2002, ISBN: 0419232001.

[2] *En 1997-1:2024, eurocode 7-geotechnical design-part 1: General rules*, European committee for standardization.

[3] R. B. Peck, "Advantages and limitations of the observational method in applied soil mechanics," *Geotechnique*, vol. 19, pp. 171–187, 2 1969, ISSN: 17517656.

[4] N. A. Hoult and K. Soga, "Sensing solutions for assessing and monitoring tunnels," *Sensor Technologies for Civil Infrastructures*, vol. 1, pp. 309–346, 2014.

[5] W. Broere, "Smart monitoring of tunnels," in *Geotechnical Aspects of Underground Construction in Soft Ground*. CRC Press, Jan. 2024, pp. 19–29, ISBN: 9781040155912.

[6] K. Soga et al., *The role of distributed sensing in understanding the engineering performance of geotechnical structures*. 2015, vol. 1, pp. 13–48, ISBN: 9780727760678.

[7] B. B.H.G and E. T. Brown, *Rock Mechanics for underground mining*, 3rd ed. Springer, 2006.

[8] E. Gerolymatou, "Notes for rock mechanics," Tech. Rep., 2019.

[9] S. V. Barrett and D. R. McCreath, "Shortcrete support design in blocky ground: Towards a deterministic approach," in *Tunnelling and Underground Space Technology incorporating Trenchless*, vol. 10, 1995, pp. 79–89.

[10] E. S. Bernard and A. H. Thomas, "Fibre reinforced sprayed concrete for ground support," *Tunnelling and Underground Space Technology*, vol. 99, p. 103 302, January 2020, ISSN: 08867798.

[11] A. Sjölander, "Structural behaviour of shotcrete in hard rock tunnels," Ph.D. dissertation, KTH Royal Institute of Technology, Sweden, 2020.

[12] L. Malmgren, "Interaction between shotcrete and rock," Ph.D. dissertation, Luleå University of Technology, Nov. 2005.

[13] Trafikverket, "Projektering av bergkonstruktioner 2014:144," Tech. Rep., 2015.

[14] E. Hoek, P. K. Kaiser, and W. F. Bawden, "Support of underground excavations in hard rock," *Support of Underground Excavations in Hard Rock*, pp. 1–213, October 2014 2000, ISSN: 1078-7275.

[15] N. Barton, R. Lien, and J. Lunde, "Engineering classification of rock masses for the design of tunnel support.," *Rock Mechanics*, pp. 189–236, 6 1974, ISSN: 01489062.

[16] V. Belloni, A. Sjölander, R. Ravanelli, M. Crespi, and A. Nascetti, "Tack project: Tunnel and bridge automatic crack monitoring using deep learning and photogrammetry," in *International Archives of the Photogrammetry, Remote Sensing and Spatial Information Sciences - ISPRS Archives*, vol. 43, 2020, pp. 741–745.

[17] U. Lindblom, "Time management of maintenance in rock tunnels for traffic," BeFo, Tech. Rep., 2012.

[18] M. Barzegar, S. Blanks, B. A. Sainsbury, and W. Timms, "Mems technology and applications in geotechnical monitoring: A review," *Measurement Science and Technology*, vol. 33, 5 May 2022, ISSN: 13616501.

[19] C. H. Dowding, M. L. Dussud, W. F. Kane, and K. M. O'connor, "Monitoring deformation in rock and soil with tdr sensor cables part 1. concept and case history," Tech. Rep., 2003, pp. 51–59.

[20] F. Tang, G. Zhou, H. N. Li, and E. Verstrynge, "A review on fiber optic sensors for rebar corrosion monitoring in rc structures," *Construction and Building Materials*, vol. 313, Dec. 2021, ISSN: 09500618.

[21] A. Güemes and B. Soller, "Optical fiber distributed sensing: Physical principles and applications," in *Structural Health Monitoring 2009: From System Integration to Autonomous Systems - Proceedings of the 7th International Workshop on Structural Health Monitoring, IWSHM 2009*, vol. 1, 2009, pp. 14–20, ISBN: 9781605950075.

[22] S. T. Kreger et al., "Optical frequency domain reflectometry: Principles and applications in fiber optic sensing," in *Fiber Optic Sensors and Applications XIII*, vol. 9852, SPIE, May 2016, 98520T, ISBN: 9781510600935.

[23] G. Rodriguez, J. R. Casas, and S. Villalba, "Shear crack width assessment in concrete structures by 2d distributed optical fiber," *Engineering Structures*, vol. 195, pp. 508–523, May 2019, ISSN: 18737323.

[24] C. G. Berrocal, I. Fernandez, and R. Rempling, "Crack monitoring in reinforced concrete beams by distributed optical fiber sensors," *Structure and Infrastructure Engineering*, vol. 17, pp. 124–139, 1 2021, ISSN: 17448980.

[25] M. Pejatović and A. Muttoni, "Experimental investigation of dowel action in reinforcing bars using refined measurements," *Structural Concrete*, vol. 25, pp. 2732–2758, 4 Aug. 2024, ISSN: 17517648.

[26] B. Forbes, N. Vlachopoulos, A. J. Hyett, and M. S. Diederichs, "A new optical sensing technique for monitoring shear of rock bolts," *Tunnelling and Underground Space Technology*, vol. 66, pp. 34–46, Jun. 2017, ISSN: 08867798.

[27] H. Mohamad, A. B. H. Kueh, and A. S. A. Rashid, "Distributed optical-fibre strain sensing in reinforced concrete structures," *Jurnal Teknologi*, vol. 74, pp. 93–97, 4 2015, ISSN: 01279696.

[28] A. Bassil, X. Chapeleau, D. Leduc, and O. Abraham, "Concrete crack monitoring using a novel strain transfer model for distributed fiber optics sensors," *Sensors (Switzerland)*, vol. 20, pp. 1–17, 8 2020, ISSN: 14248220.

[29] A. Deif, B. Martín-Pérez, B. Cousin, C. Zhang, X. Bao, and W. Li, "Detection of cracks in a reinforced concrete beam using distributed brillouin fibre sensors," *Smart Materials and Structures*, vol. 19, 5 2010, ISSN: 09641726.

[30] T. Liu, H. Huang, and Y. Yang, "Crack detection of reinforced concrete member using rayleigh-based distributed optic fiber strain sensing system," *Advances in Civil Engineering*, vol. 2020, 2020, ISSN: 16878094.

[31] C. G. Berrocal, I. Fernandez, M. F. Bado, J. R. Casas, and R. Rempling, "Assessment and visualization of performance indicators of reinforced concrete beams by distributed optical fibre sensing," *Structural Health Monitoring*, vol. 20, pp. 3309–3326, 6 Nov. 2021, ISSN: 17413168.

[32] I. Fernandez, C. G. Berrocal, S. Almfeldt, and R. Rempling, "Monitoring of new and existing stainless-steel reinforced concrete structures by clad distributed optical fibre sensing," *Structural Health Monitoring*, vol. 22, pp. 257–275, 2023.

[33] I. Fernandez, C. G. Berrocal, M. Johansson, M. Roupe, and R. Rempling, "Enhanced digital twin for on-site inspections using distributed optical fiber sensors and augmented reality," *Automation in Construction*, vol. 181, Jan. 2026, ISSN: 09265805.

[34] S. Villalba and J. R. Casas, "Application of optical fiber distributed sensing to health monitoring of concrete structures," *Mechanical Systems and Signal Processing*, vol. 39, pp. 441–451, 1-2 2013, ISSN: 08883270.

[35] A. Barrias, J. R. Casas, and S. Villalba, "A review of distributed optical fiber sensors for civil engineering applications," *Sensors (Switzerland)*, vol. 16, 5 2016, ISSN: 14248220.

[36] R. Regier and N. A. Hoult, "Distributed strain behavior of a reinforced concrete bridge: Case study," *Journal of Bridge Engineering*, vol. 19, p. 05 014 007, 12 2014, ISSN: 1084-0702.

[37] A. Brault, N. A. Hoult, T. Greenough, and I. Trudeau, "Monitoring of beams in an rc building during a load test using distributed sensors," *Journal of Performance of Constructed Facilities*, vol. 33, p. 04 018 096, 1 2019, ISSN: 0887-3828.

[38] A. A. Chávez, J. Gonzalez-Libreros, L. Elfgren, G. S. Luleå, L. Capacci, and F. Biondini, "Structural model updating of an existing concrete bridge based on load testing and monitoring data," in *Life-Cycle of Structures and Infrastructure Systems - Proceedings of the 8th International Symposium on Life-Cycle Civil Engineering, IALCCE 2023*, CRC Press/Balkema, 2023, pp. 3999–4006, ISBN: 9781003323020.

[39] C. M. Monsberger, W. Lienhart, and M. Hayden, "Distributed fiber optic sensing along driven ductile piles: Design, sensor installation and monitoring benefits," *Journal of Civil Structural Health Monitoring*, vol. 10, pp. 627–637, 4 2020, ISSN: 21905479.

[40] G.-B. Shin et al., "Distributed fiber optic sensing for monitoring piles under eccentric load," *Journal of Geotechnical and Geoenvironmental Engineering*, vol. 152, 9 Sep. 2026, ISSN: 1090-0241.

[41] L. Gao, J. Qian, C. Han, S. Qin, and K. Feng, "Experimental study of deformation measurement of bored pile using ofdr and botdr joint optical fiber sensing technology," *Sustainability (Switzerland)*, vol. 14, 24 Dec. 2022, ISSN: 20711050.

[42] H. Mohamad, A. A. A. Beddelee, M. F. Ghazali, H. E. Lee, K. Chaiyasarn, and M. Y. M. Nasir, "Distributed fibre optic inclinometer with cloud-based monitoring system," *Engineering Science and Technology, an International Journal*, vol. 41, May 2023, ISSN: 22150986.

[43] C. C. Zhang, H. H. Zhu, S. P. Liu, B. Shi, and D. Zhang, "A kinematic method for calculating shear displacements of landslides using distributed fiber optic strain measurements," *Engineering Geology*, vol. 234, pp. 83–96, Feb. 2018, ISSN: 00137952.

[44] H. Pei, F. Zhang, H. Zhu, J. Liu, F. Ning, and W. Chen, "Development of a distributed three-dimensional inclinometer based on ofdr technology and the frenet-serret equations," *Measurement: Journal of the International Measurement Confederation*, vol. 223, Dec. 2023, ISSN: 02632241.

[45] E. Damiano et al., "Innovative extenso-inclinometer for slow-moving deep-seated landslide monitoring in an early warning perspective," *Journal of Rock Mechanics and Geotechnical Engineering*, 2025, ISSN: 25890417.

[46] T. P. Roper, B. Forbes, and J. Karlovšek, "The application of distributed optical strain sensing to measure rock bolt deformation subject to bedding shear," *World Academy of Science, Engineering and Technology International Journal of Geotechnical and Geological Engineering*, vol. 14, pp. 86–92, 2 2020.

[47] A. Jansson, C. G. Berrocal, R. Rempling, and I. Fernandez, "Detecting and quantifying shear fault displacements during tunnelling in hard rock using distributed optical fibre sensors," in *Bergdagarna 2025*, Jan. 2025.

[48] A. Jansson, C. Berrocal, R. Rempling, and I. Fernandez, "Monitoring of shear deformations in hard rock discontinuities using distributed optical fibre sensors," in *Tunnelling into a Sustainable Future – Methods and Technologies*, CRC Press, May 2025, pp. 3969–3976.

[49] C. Y. Gue, M. Wilcock, M. M. Alhaddad, M. Z. Elshafie, K. Soga, and R. J. Mair, "Monitoring the effects of tunnelling under an existing tunnel-fibre optics," *Geotechnical Aspects of Underground Construction in Soft Ground - Proceedings of the 8th Int. Symposium on Geotechnical Aspects of Underground Construction in Soft Ground, TC204 ISSMGE - IS-SEOUL 2014*, pp. 357–361, 2014.

[50] J. Gómez, J. R. Casas, and S. Villalba, "Structural health monitoring with distributed optical fiber sensors of tunnel lining affected by nearby construction activity," *Automation in Construction*, vol. 117, p. 103 261, December 2019 2020, ISSN: 09265805.

[51] A. Barrias, G. Rodriguez, J. R. Casas, and S. Villalba, "Application of distributed optical fiber sensors for the health monitoring of two real structures in barcelona," *Structure and Infrastructure Engineering*, vol. 14, pp. 967–985, 7 2018, ISSN: 17448980.

[52] X. Zhang and W. Broere, "Design of a distributed optical fiber sensor system for measuring immersed tunnel joint deformations," *Tunnelling and Underground Space Technology*, vol. 131, Jan. 2023, ISSN: 08867798.

[53] X. Zhang, H. Zhu, X. Jiang, and W. Broere, *Distributed fiber optic sensors for tunnel monitoring: A state-of-the-art review*, Sep. 2024.

[54] N. D. Battista, M. Elshafie, K. Soga, M. Williamson, G. Hazelden, and Y. S. Hsu, "Strain monitoring using embedded distributed fibre optic sensors in a sprayed concrete tunnel lining during the excavation of cross-passages," in *SHMII 2015 - 7th International Conference on Structural Health Monitoring of Intelligent Infrastructure*, 2015.

[55] C. M. Monsberger and W. Lienhart, "Distributed fiber optic shape sensing along shotcrete tunnel linings: Methodology, field applications, and monitoring results," *Journal of Civil Structural Health Monitoring*, vol. 11, pp. 337–350, 2 2021, ISSN: 21905479.

[56] C. M. Monsberger, W. Lienhart, A. Kluckner, L. Wagner, and W. Schubert, "Continuous strain measurements in a shotcrete tunnel lining using distributed fibre optic sensing," *9th European Workshop on Structural Health Monitoring, EWSHM 2018*, July 2018.

[57] L. Courard, T. Piotrowski, and A. Garbacz, "Near-to-surface properties affecting bond strength in concrete repair," *Cement and Concrete Composites*, vol. 46, pp. 73–80, 2014, ISSN: 09589465.

[58] N. Grant, R. Ratcliffe, and F. Papworth, "Design guidelines for the use of sfrs in ground support," *Shotcrete: Engineering Developments*, pp. 111–118, January 2002 2002.